

High-frequency readout free from transmon multi-excitation resonances

Pavel D. Kurilovich,^{1,*} Thomas Connolly,^{1,*} Charlotte G. L. Böttcher,^{1,†} Daniel K. Weiss,^{1,2,‡} Sumeru Hazra,¹ Vidul R. Joshi,^{1,§} Andy Z. Ding,¹ Heekun Nho,¹ Spencer Diamond,¹ Vladislav D. Kurilovich,^{1,¶} Wei Dai,¹ Valla Fatemi,^{1,3} Luigi Frunzio,¹ Leonid I. Glazman,^{1,2} and Michel H. Devoret^{1,**}

¹*Departments of Applied Physics and Physics, Yale University, New Haven, Connecticut 06520, USA*

²*Yale Quantum Institute, Yale University, New Haven, Connecticut 06511, USA*

³*School of Applied and Engineering Physics, Cornell University, Ithaca, New York 14853, USA*

Quantum computation will rely on quantum error correction to counteract decoherence. Successfully implementing an error correction protocol requires the fidelity of qubit operations to be well-above error correction thresholds [1, 2]. In superconducting quantum computers, measurement of the qubit state remains the lowest-fidelity operation [3]. For the transmon, a prototypical superconducting qubit, measurement is carried out by scattering a microwave tone off the qubit. Conventionally, the frequency of this tone is of the same order as the transmon frequency. The measurement fidelity in this approach is limited by multi-excitation resonances in the transmon spectrum which are activated at high readout power [4–10]. These resonances excite the qubit outside of the computational basis, violating the desired quantum non-demolition character of the measurement. Here, we find that strongly detuning the readout frequency from that of the transmon exponentially suppresses the strength of spurious multi-excitation resonances. By increasing the readout frequency up to twelve times the transmon frequency, we achieve a quantum non-demolition measurement fidelity of 99.93% with a residual probability of leakage to non-computational states of only 0.02%.

I. INTRODUCTION

Many quantum error correction protocols, such as the surface code [11], check for errors by repeatedly measuring a subset of qubits [3, 12–17]. These error checks should not introduce additional errors, which imposes two stringent requirements on the measurement. First, the measurement must project the system onto an eigenstate of the observed quantity. Second, the eigenstate must be successfully identified. A measurement that satisfies these criteria is called quantum non-demolition (QND) [18]. Achieving a high-fidelity QND qubit measurement remains one of the outstanding challenges in performing real-time quantum error correction across different quantum computing platforms [3, 19–21].

In circuit quantum electrodynamics, qubit measurement is carried out by scattering non-resonant microwaves off the qubit and analyzing the amplified [22–31] scattered signal [32–40]. Information about the state of the qubit is encoded in the amplitude and phase of the scattered signal, see Fig. 1(a). Since the readout tone in such a dispersive readout is not resonant with the qubit,

the measurement should not cause transitions between energy eigenstates. Thus, dispersive measurement can in principle be QND. One limitation on the QND character of the readout comes from the possibility of qubit decay during the measurement [41]. This limitation can be overcome by increasing the measurement speed, which requires increasing the power of the readout tone.

However, there is experimental evidence that dispersive readout loses its QND character at high powers [4, 5, 35, 37, 39, 42]. Transmons [43, 44], the most commonly used superconducting qubits, get excited to higher non-computational states by strong readout tones. It is believed that this happens due to the non-linear absorption of readout photons [6–10]. In this process, a few photons from the readout tone are simultaneously absorbed by the transmon, causing it to “leak” to a non-computational state. Nonlinear absorption can be resonant even when the readout frequency is detuned from the qubit transition frequency. Problematically, the strength of multi-excitation resonances, and thus the leakage probability, sharply increases with the power of the readout tone. Error correction protocols are designed to correct only for bit-flip and phase-flip errors, not leakage errors [45–53]. Multi-excitation resonances thus must be eliminated for quantum computation to operate. Is it possible to avoid the activation of transmon multi-excitation resonances and implement high-fidelity QND qubit readout?

In this article, we answer this question affirmatively by demonstrating a dispersive transmon readout free of significant multi-excitation resonances. We achieve this by using a readout resonator with a frequency ω_r exceeding that of the transmon, ω_q , by a factor of 12, see Fig. 1(b). The strong frequency mismatch greatly reduces the number of relevant multi-excitation resonances compared to

* These two authors contributed equally.

pavel.kurilovich@yale.edu, tom.connolly@yale.edu

† Present address: Department of Applied Physics, Stanford University, Stanford, California 94305, USA

‡ Present address: Quantum Circuits, Inc., New Haven, CT, USA

§ Present address: Microsoft Quantum

¶ Present address: Google Quantum AI, 301 Mentor Dr, Goleta, CA93111, USA

** michel.devoret@yale.edu

Present address: Physics Dept., U.C. Santa Barbara, Santa Barbara, California 93106, USA and Google Quantum AI, 301 Mentor Dr, Goleta, California 93111, USA

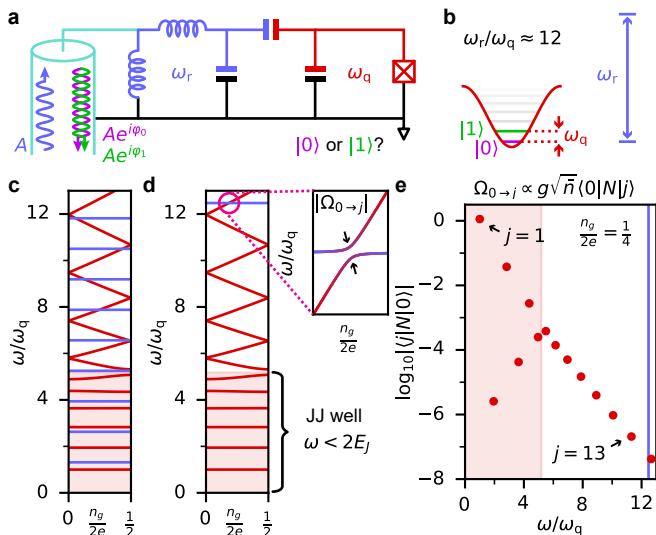


FIG. 1. (a) Readout of a transmon (red) is achieved by monitoring the signal reflected from the readout resonator (blue). The information about the transmon state is encoded in the phase of the reflected signal. (b) In our experiment, the frequency of the readout resonator exceeds that of the transmon roughly by a factor of 12. (c) Transition spectrum of the system in the standard readout regime, $\omega_r \sim \omega_q$. Red lines show transition frequencies from the ground state $|0\rangle$ of the transmon as a function of the offset charge n_g . The shaded region indicates transitions to states within the Josephson energy well. Blue lines correspond to n -photon transitions of the readout resonator. The number of accidental spectral collisions between the transmon and the readout resonator is large. These collisions are responsible for the undesired transmon excitation to non-computational states. (d) In the regime $\omega_r \gg \omega_q$, the number of spectral collisions is greatly reduced. Inset: the resonator transition anti-crosses with a transmon transition to a highly lying state $|j\rangle$. The strength Ω of this anti-crossing is proportional to the matrix element of the transmon charge operator N . (e) Numerically calculated matrix element $\langle 0|N|j\rangle$ for different final states $|j\rangle$ as a function of the transition frequency $\omega = E_{j0}/\hbar$. The matrix element is exponentially suppressed with increasing ω/ω_q . The blue line corresponds to the resonator frequency.

the standard regime $\omega_r \sim \omega_q$, see Figure 1(c,d). The matrix elements for the remaining resonances are exponentially suppressed in the large parameter ω_r/ω_q , see Fig. 1(e). Operating in this limit allows us to achieve a readout with a QND fidelity of 99.93%. The remaining readout error stems from mechanisms unrelated to multi-excitation resonances in the transmon spectrum. The investigation of these mechanisms will be presented in a separate work [54].

The suppression of the qubit decay via the Purcell effect is the additional benefit of a highly detuned readout resonator. Specifically, the Purcell decay rate is reduced by an additional factor of $(\omega_r/\omega_q)^3$ compared to the standard readout regime, $\omega_r \sim \omega_q$ [55]. In fact, our readout result is achieved without a Purcell filter [36, 56], yet our

qubit lifetime is not limited by the Purcell effect. Eliminating the Purcell filter reduces the hardware overhead associated with qubit measurement in quantum processors.

The novel readout technique that we demonstrated can be used for sensing applications where precise non-demolition measurement is desirable. These include search for dark matter [57–59] and detection of single spins [60–63]. High-frequency readout can also be used to robustly probe transmons with exotic Josephson junctions [64, 65] where the qubit frequency can vary strongly with parameters. Additionally, a high-frequency drive could be employed to avoid undesired multi-excitation resonances in applications other than measurement. Among them are two-qubit gates [66], quantum control of linear oscillators [16, 67], and Floquet-engineering [68] of superconducting circuit Hamiltonians.

II. CONCEPT DESCRIPTION

In dispersive readout, a transmon qubit is capacitively coupled to a readout resonator, see Fig. 1(a). Due to the transmon non-linearity, the frequency of the resonator shifts by χ when the transmon is excited from its ground state $|0\rangle$ to the first excited state $|1\rangle$. By measuring the phase of the signal reflected from the resonator, it is then possible to infer the transmon state. When $\omega_r \gg \omega_q$, the dispersive shift is given by

$$\hbar\chi = -8E_C(g/\omega_r)^2, \quad (1)$$

where g is the resonator-transmon coupling strength and E_C is the charging energy of the transmon. Note that this expression for the dispersive shift differs from its familiar form in the case of a nearly-resonant readout [43]. We derive this new expression in the supplementary materials [55]. Notably, in the regime $\omega_r \gg \omega_q$, it is important to account for the counter-rotating terms in transmon-resonator coupling Hamiltonian to correctly compute the dispersive shift. The contribution of these terms was previously discussed in [69]. In fact, in our regime the dispersive shift is enhanced roughly by a factor of four compared to the standard result of Ref. [43] computed for the same ratio of g and detuning $|\omega_r - \omega_q|$.

The rate at which we obtain information about the transmon state during readout is proportional to the dispersive shift and the number of photons in the resonator, $\Gamma_{\text{meas}} \propto \bar{n}\chi$ [70]. The number of photons \bar{n} in the readout resonator scales linearly with the power of the readout tone. The measurement speed can thus be increased by increasing the readout power.

However, increasing the power of the readout tone can activate multi-excitation resonances in the transmon spectrum, which may be detrimental for QND readout. When $\omega_r \gg \omega_q$, the strongest allowed resonance employs a single readout photon to excite the transmon from an initial computational state $|i\rangle$ to a final highly excited state $|j\rangle$. This process is possible if the frequency

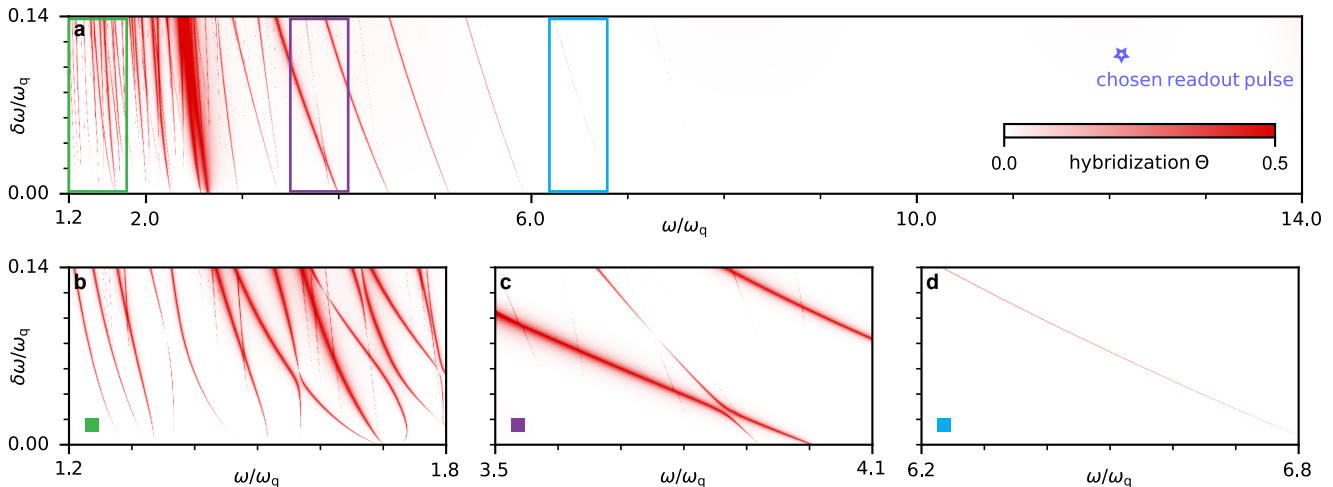


FIG. 2. Numerically simulated landscape of multi-excitation resonances for a transmon with $E_J/E_C = 60$ at offset charge $n_g = 0.25$. The horizontal axis shows the normalized drive frequency and the vertical axis shows the normalized drive power (quantified by the AC Stark shift $\delta\omega$ of the qubit transition). The color shows the degree of hybridization Θ between the computational state $|1\rangle$ and the non-computational states; multi-excitation resonances correspond to the regions where this hybridization is enhanced. Specifically, dimensionless number Θ corresponds to the probability of finding the system outside of the computational subspace due to accidental Rabi processes involving the non-computational states. Away from multi-excitation resonances $\Theta = 0$, on any of the isolated resonances $\Theta = 1/2$. (a) Multi-excitation resonances in a broad frequency range. The blue star shows the frequency and the average drive power of our chosen readout pulse. (b)-(d) Zoom in on three frequency windows highlighted with colored boxes in panel (a). (b) Standard regime of the transmon readout, $\omega \sim \omega_q$. Multi-excitation resonances quickly become dense with the increase of power. (c,d) As the frequency is increased, both the number of the multi-excitation resonances and the corresponding transition amplitudes are progressively suppressed.

matching condition $\omega_r = E_{ji}/\hbar = (E_j - E_i)/\hbar$ is fulfilled (here, E_j and E_i are the energies of the final and initial state, correspondingly). The frequency matching condition suggests that it may be possible to fine-tune the spectrum of the system to avoid undesired resonances. In practice, this strategy is complicated by two factors. First, energies E_j and E_i experience an AC Stark shift. The Stark shift depends on the number of photons in the cavity \bar{n} , which varies with time during the readout. Therefore, E_{ji}/\hbar sweeps a range of frequencies. Second, the energy E_j might vary significantly with the offset charge of the transmon, see Fig. 1(d). Random drift of the offset charge with time makes it hard to avoid the resonances.

Fortunately, the transition amplitude of the multi-excitation resonance can be suppressed *exponentially* by increasing ω_r/ω_q . To see this, we note that as ω_r is increased, an undesired transition to a progressively higher final state $|j\rangle$ becomes resonant with the readout tone. The transition amplitudes for these successive resonances are given by $\Omega_{i \rightarrow j} \propto g\sqrt{\bar{n}}N_{ji}/N_{zpf}$, where $N_{ji} = |\langle j|N|i\rangle|$ is the matrix element of the transmon charge operator and N_{zpf} is its zero-point fluctuation [71]. Our theoretical result for N_{ji} for different final states is shown in Figure 1(e). It demonstrates the exponential decrease of N_{ji} with ω_r/ω_q . This decrease allows us to strongly suppress the multi-excitation resonances by increasing the readout frequency. The weaker power-law reduction of

the dispersive shift resulting from the increase of ω_r can be compensated to an extent by increasing the coupling strength g .

To further illustrate the suppression of multi-excitation resonances for the high-frequency readout, we numerically evaluate the resonant frequencies and the corresponding transition amplitudes as a function of drive power. We do this by calculating the Floquet modes of a driven transmon Hamiltonian $H = 4E_C(N - n_g)^2 - E_J \cos \varphi + \hbar\zeta N \cos(\omega t)$, where E_J is the Josephson energy of the transmon and φ is its superconducting phase. The drive term with amplitude ζ and frequency ω models [72] the readout tone [6–9]. We then evaluate the hybridization between the computational state $|1\rangle$ and the non-computational excited states at different ω and ζ , see Figure 2. The multi-excitation resonances can be identified as regions where this hybridization is enhanced. We quantify the drive power by the AC Stark shift $\delta\omega = \bar{n}\chi$ experienced by the qubit; this metric can be expressed in terms of the drive amplitude ζ as $\delta\omega/\omega_q = \frac{1}{8}\omega^2\zeta^2/(\omega^2 - \omega_q^2)^2$ where we assumed $E_C \ll E_J, \hbar|\omega_r - \omega_q|$. In the context of transmon readout, the Stark shift directly quantifies the rate Γ_{meas} of acquiring the information about the qubit state [73]. The details of the numerical procedure and a similar analysis for the transmon state $|0\rangle$ are presented in the supplementary materials [55]. In Figure 2 we chose the value of the offset charge $n_g = 0.25$ as an illustrative example; vari-

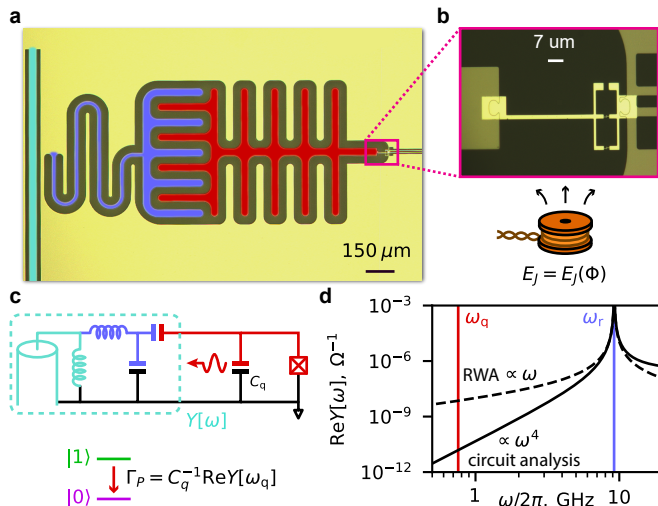


FIG. 3. (a) False-colored microscope image of the device. A transmon with frequency $\omega_q/2\pi = 0.758$ GHz (red) is capacitively coupled to a readout resonator with frequency $\omega_r/2\pi = 9.227$ GHz (blue). The resonator is inductively coupled to the readout transmission line (turquoise). (b) Zoom in on the region containing the Josephson junctions (see Figure S2 of the supplementary materials [55] for details). The Josephson energy of the transmon can be tuned by threading flux through the SQUID loop. A third (upper) arm of the SQUID is electrically open and is not used in this experiment. (c) The decay rate of transmon excitations into the transmission line, Γ_P , is proportional to the dissipative part $\text{Re}Y[\omega_q]$ of the environment admittance at the transmon frequency. (d) The frequency dependence of $\text{Re}Y[\omega]$ corresponding to the circuit in the previous panel (solid line). In the regime $\omega_r \gg \omega_q$, the Purcell decay is suppressed by several orders of magnitude compared to the standard formula obtained within rotating wave approximation, $\Gamma_P^{\text{RWA}} = \kappa g^2 / \Delta^2$ (dashed line).

ation of the multi-excitation resonances with n_g is also explored in the supplementary materials.

It is apparent from the figure that in the standard regime of readout frequencies, $\omega \sim \omega_q$, the multi-excitation resonances are dense and have large transition amplitudes. In contrast, when $\omega \gg \omega_q$ both the number and the strength of the resonances are strongly suppressed. This makes multi-excitation resonances irrelevant for the readout performance. The decrease in the number of spurious resonances with the increase of drive frequency is noted in some of the numeric simulations presented in Ref. [8].

III. EXPERIMENTAL SETUP

To experimentally demonstrate the advantage of high-frequency transmon readout, we realized a device with a readout resonator with frequency $\omega_r/2\pi = 9.227$ GHz and a transmon with frequency $\omega_q/2\pi = 0.758$ GHz, such that $\omega_r/\omega_q \approx 12$, see Figure 3. We chose to reduce the

transmon frequency from its typical value of several GHz and keep the readout in the standard range so that we can use our existing microwave components and electronics in the readout chain. The measured excited state probability $p_1 = 3\%$ corresponds to an effective temperature of $T_q = 11$ mK. The charging energy of the transmon is $E_C/h = 36$ MHz, and the Josephson energy is $E_J/h = 2.2$ GHz. The large detuning between the transmon and the resonator forces us to couple them strongly to obtain an appreciable resonator dispersive shift, such that $g \sim \omega_q$. A large interdigitated coupling capacitor in a 2D geometry results in $g/2\pi = 0.515$ GHz and $\chi/2\pi = 0.90$ MHz [74]. For an efficient readout, the coupling between the resonator and the transmission line κ should be comparable to the dispersive shift χ . For our inductively-coupled resonator, $\kappa/2\pi = 1.80$ MHz.

A Purcell filter [56] was not necessary in our setup, despite the strong coupling between the qubit and the readout resonator. Taking the standard result for the qubit decay rate due to the Purcell effect [32, 75–78], $\Gamma_P^{\text{RWA}} = \kappa \cdot (g/\Delta)^2$, we find that the lifetime of our qubit should be limited to $30 \mu\text{s}$ (here, $|\Delta| = \omega_r - \omega_q \approx \omega_r$). This is in stark contrast with the measured value of $T_1 = 388 \mu\text{s}$. The discrepancy arises because the approximations used in the derivation of Γ_P^{RWA} are not justified in the regime $\omega_r \gg \omega_q$. The standard result for the Purcell decay rate neglects the frequency dependence of the transmon-resonator and resonator-transmission line coupling impedances. This is reasonable when $|\omega_r - \omega_q| \ll \omega_r$, but not when $\omega_q \ll \omega_r$. For example, at small frequencies the resonator-transmission line coupling inductor more effectively shunts the transmission line. These effects modify the expression for the decay rate to $\Gamma_P = \kappa \cdot 4(\omega_q/\omega_r)^3 (g/\omega_r)^2$ [55]. The corresponding bound on the qubit lifetime, $T_1^P = 11$ ms, vastly exceeds the measured T_1 . We believe that the lifetime of our qubit is limited by the material properties. We note that the deviations from the standard Purcell formula were recently discussed in Ref. [79].

We readout the transmon state by sending a microwave pulse to the readout resonator. Upon reflecting from the resonator, the pulse acquires information about the qubit state. The pulse is then routed through a series of amplifiers. The first amplifier in the chain is a near-quantum limited SNAIL parametric amplifier [28] (SPA) operated in phase-sensitive mode which allows us to achieve a measurement efficiency of 89%. The amplified signal is then demodulated and digitized by room-temperature measurement electronics. The digitized signal is integrated using an envelope that maximizes the signal-to-noise ratio [41, 80]. We assign a state $|0\rangle$ or $|1\rangle$ to the outcome of the measurement based on whether it is closer to the average outcome for $|0\rangle$ or $|1\rangle$, respectively.

The readout operation is considered to be complete when the resonator is sufficiently empty of readout photons such that the qubit no longer experiences significant dephasing. To speed up the measurement, we employ a shaped readout pulse which is designed to leave the read-

out resonator empty of photons at the end of the measurement [42, 81]. This allows us to avoid waiting for the readout photons to leak out of the resonator spontaneously, which would take much longer than the cavity decay time. The pulses are numerically optimized to maximize the discernibility of $|0\rangle$ and $|1\rangle$ while keeping the time-integrated number of photons in the resonator fixed. Simulated trajectories of the resonator field under the action of our readout pulse for two transmon states are shown in Figure 4. Notably, to accurately deplete the resonator of photons, it is important to take into account the Kerr nonlinearity of the resonator.

IV. QND FIDELITY

Ideally, the dispersive measurement described above results in a QND readout of the qubit state. In reality, the performance of the readout is limited by two imperfections. First, noise in the readout signal can lead to a state assignment error, where the measurement outcome for a qubit in state $|1\rangle$ falls on the side of the threshold corresponding to state $|0\rangle$ (or vice versa). Second, the transmon can experience a transition error where its state changes during the readout. For example, state $|1\rangle$ can decay to $|0\rangle$ during the readout pulse. The QND fidelity \mathcal{Q} is correspondingly given by

$$1 - \mathcal{Q} = \varepsilon_{\text{assign}} + \varepsilon_{\text{trans}} \quad (2)$$

with $\varepsilon_{\text{assign}}$ being the misassignment probability and $\varepsilon_{\text{trans}}$ being the transition probability [55]. Here, we average \mathcal{Q} over the computational qubit states $|0\rangle$ and $|1\rangle$. Both types of errors should be minimized to obtain a near-unity QND fidelity.

However, minimization of $\varepsilon_{\text{trans}}$ is in conflict with minimization of $\varepsilon_{\text{assign}}$. The noise in the readout signal cannot be reduced below limits set by the Heisenberg uncertainty principle, so the assignment error can only be reduced by increasing the power or duration of the readout. Increasing the duration is undesirable because the transmon would have more time to decay, which increases transition errors. One would hope to reduce both $\varepsilon_{\text{assign}}$ and $\varepsilon_{\text{trans}}$ by using a short pulse with a high power. However, it is not possible to increase \mathcal{Q} indefinitely by increasing the power of the drive because high-power drives themselves induce state transitions. Such drive-induced transitions ultimately bound the achievable QND fidelity.

Our goal is to optimize the QND fidelity as a function of readout power and duration. To this end, we measure $\varepsilon_{\text{assign}}$ and $\varepsilon_{\text{trans}}$ as a function of pulse parameters. To measure $\varepsilon_{\text{assign}}$ and $\varepsilon_{\text{trans}}$, we prepare the qubit in either $|0\rangle$ or $|1\rangle$ and then perform a series of back-to-back measurements to check the consistency of the results. Assuming that the errors are rare and independent, we can readily identify both assignment errors and transition errors. When the assignment changes from consistently $|0\rangle$ to consistently $|1\rangle$ or vice versa, we conclude a transition error occurred, see upper panel in Figure 4(b). When

one measurement in the middle of the sequence disagrees with the measurements before and after, we identify an assignment error, see lower panel in Figure 4(b).

There is, however, an important complication in this protocol due to the possibility of leakage to non-computational transmon states. Our readout is only effective at distinguishing states $|0\rangle$ and $|1\rangle$ from each other; non-computational states are mistakenly assigned to either $|0\rangle$ or $|1\rangle$. Because of this, the protocol described above does not correctly quantify the probability of transition errors to leakage states. Moreover, leakage corrupts further measurements in the sequence. While the outcomes of corrupted measurements are still assigned to $|0\rangle$ or $|1\rangle$, the statistics of these outcomes do not contain information about the discrimination of computational states.

In order to remedy this problem, we interleave repeated qubit measurement sequences with leakage checks. These checks are dispersive measurements performed using a different frequency of the readout tone. They can distinguish the non-computational states from the computational ones, but are not effective at distinguishing $|0\rangle$ from $|1\rangle$ [55]. The leakage checks allow us to both quantify the transition probability to non-computational states and to discard the sequences where the transmon starts from a non-computational state when computing the QND fidelity. The resulting protocol for measuring the QND fidelity is summarized in Figure 4.

To find the maximum achievable QND fidelity, we sweep the power and duration of the readout pulse. For a fixed pulse duration, at small power, the QND fidelity is limited by assignment errors, see Figure 4(d). Increasing the power exponentially suppresses $\varepsilon_{\text{assign}}$. At higher powers, the readout induces leakage to non-computational states and increases $\varepsilon_{\text{trans}}$. Finding a balance between the assignment errors and the drive-induced transition errors determines the optimal power for a fixed pulse duration. As expected, reducing the pulse duration decreases the probability of transitions between $|0\rangle$ and $|1\rangle$, see Figure 4(e), but requires more power for a fixed $\varepsilon_{\text{assign}}$. The increase of the optimal power for shorter pulses leads to an increased probability of leakage errors, setting a limit on how short the optimal pulse is.

Notably, the drive-induced leakage error that we see is unrelated to multi-excitation resonances. In our system, such resonances would excite the transmon to states outside of the Josephson well; see Figure 1. In contrast, leakage checks reveal that the dominant drive-induced leakage process excites the transmon to low-lying non-computational states $|2\rangle$ and $|3\rangle$, see supplementary materials [55]. This occurs due to inelastic scattering of readout photons into the transmon environment. We will describe this process in a separate publication [54].

As a result of optimization, we obtain a maximum QND fidelity of 99.93% using a 320 ns-long pulse with a maximum AC Stark shift on the qubit $\delta\omega/\omega_q = 0.11$. This Stark shift corresponds to 92 photons in the readout

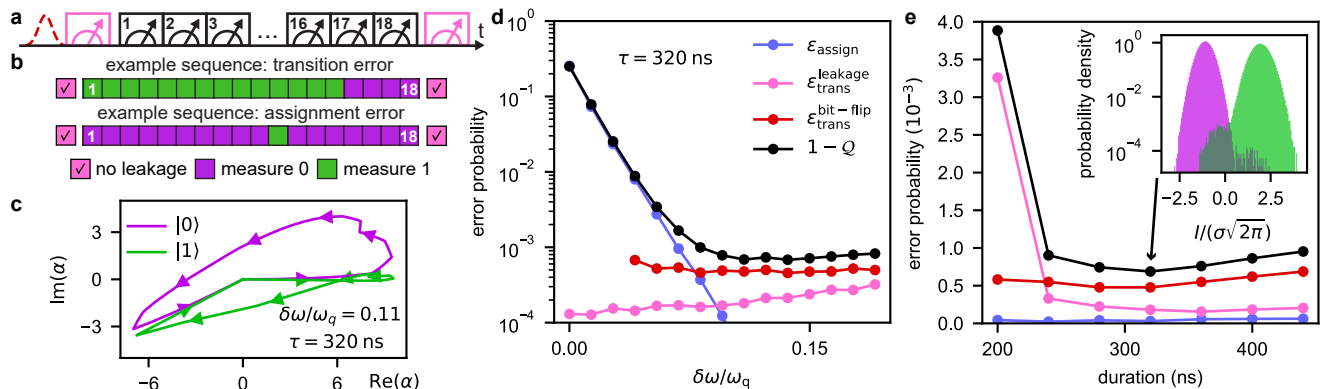


FIG. 4. Measurement of QND fidelity. (a) Experimental sequence used to estimate QND fidelity. A π -pulse (red) is played before the beginning of the sequence half the time. 18 back-to-back qubit measurements (black) are performed between a pair of leakage check measurements (pink). (b) Examples of series of measurement outcomes in which one of the measurements contains an error. In the upper panel, a transition error is identified by a sustained switch in state assignment upon repeated measurements. In the lower panel, an assignment error is identified as an isolated change in state assignment. (c) Numerically simulated resonator coherent state trajectories for a shaped readout pulse designed to empty the cavity of readout photons at the end of the pulse irrespective of the qubit state. The pulse is numerically optimized to maximize the SNR while keeping the number of photons in the resonator small. (d) Error probability as a function of readout power when using a 320 ns readout pulse. We separately show the probability of assignment error ϵ_{assign} , transition error where a transition between $|0\rangle$ and $|1\rangle$ happens, $\epsilon_{\text{trans}}^{\text{bit-flip}}$, and transition error where a transition to non-computational states happens, $\epsilon_{\text{trans}}^{\text{leakage}}$. (e) Error probability as a function of pulse duration. For each duration, the readout power is chosen to maximize the QND fidelity. The optimal pulse has a duration of 320 ns, $Q = 99.93\%$, and leakage probability of 0.02%. Inset: histograms of integrated measurement signal for transmon initialized in states $|0\rangle$ and $|1\rangle$. The measurement is performed with the optimal pulse and the histograms are conditioned on the absence of leakage.

resonator. To the best of our knowledge, the error in the QND fidelity that we measure is about an order of magnitude smaller than the previous state-of-the-art result for superconducting qubits [39, 40, 42]. This improvement, obtained with a drive power far exceeding that of past experiments, results from the absence of transmon multi-excitation resonances. The probability of leakage per readout that we observe does not exceed 0.02%. The state assignment fidelity, another commonly used readout metric, is at least as large as Q [55].

Finally, we note that our shaped readout pulses are effective at emptying the readout resonator of photons once the readout is completed. Our optimized highest-fidelity readout pulse leaves less than 0.04 photons in the readout resonator at the end of the pulse on average, regardless of the initial transmon state. See supplementary materials for more details [55]. We leave further improvement of the emptying of the resonator for future work.

V. CONCLUSION

Conventionally, in dispersive transmon measurement, the frequency of the readout resonator is of the same order as the qubit frequency. To improve the QND character of the measurement, one can increase the power of the readout signal. However, if the power becomes too large, the signal can activate multi-excitation resonances which eject the transmon out of the computational basis.

This process has so far limited the readout performance for superconducting qubits and remained an important hurdle for quantum error correction.

We demonstrated that unwanted resonances can be eliminated from dispersive transmon measurement by increasing the readout frequency. By separating the transmon and resonator frequencies by over an order of magnitude, we achieved a beyond state-of-the-art readout which retains a QND character with a probability of 99.93%. This achievement sets readout fidelity on par with other qubit operations in superconducting quantum computing. The remaining QND error that we observe is not related to transmon multi-excitation resonances. It stems predominantly from transmon decay during the readout and its excitation outside of the computational basis in the process of inelastic scattering of readout photons [54]. The probability of leakage to non-computational states per readout does not exceed 0.02%.

In our work, the transmon has an unusual small frequency of $\omega_q/2\pi = 0.758$ GHz. This allowed us to use a conventional readout resonator frequency $\omega_r/2\pi = 9.227$ GHz while keeping the ratio ω_r/ω_q high. At face value, quantum computation with such low-frequency transmons seems to encounter two challenges: significant thermal population ($p_1 \sim 3\%$ in our experiment) and slow gate speed limited by reduced transmon anharmonicity.

We believe that neither of these factors pose a significant limitation. The thermal population can be straight-

forwardly constrained using either measurement-based feedback or an unconditional reset [49, 82]. While the small anharmonicity does limit the gate speed, the lifetime of our qubit also exceeds that of most transmons in the conventional frequency range. This suggests that the gate fidelity can be kept high despite the slow gate speed. In fact, assuming that the decoherence comes from lossy dielectric materials, the transmon quality factor does not depend on its frequency. This would imply that the fidelities of qubit gates should also be frequency-independent. The only drawback would be a reduced rate of the absolute processor speed. We leave the experimental demonstration of this principle for future work.

Alternatively, one could use a transmon in the typical frequency range of several GHz and an unusually high frequency readout resonator. This would strongly suppress the thermal population in both the transmon and the readout resonator. Increasing the readout frequency may prove useful, since the transmission line temperature becomes elevated when the line is driven strongly [83]. The resulting thermal photons in the readout resonator dephase the qubit.

VI. ACKNOWLEDGEMENTS

We thank Christian K. Andersen, Arno Bargerbos, Marta Pita-Vidal, Lukas Splitthoff, Jaap Wesdorp, and

Daniel Sank for discussions. We thank Alessandro Mi-ano and Elifnaz Önder for help with the measurement setup. We thank Jayameenakshi Venkatraman, Xu Xiao, and Rodrigo G. Cortiñas for discussions of Floquet simulations. We thank Daniil Antonenko for discussions of pulse optimization. Finally, we thank Y. Sun, K. Woods, L. McCabe, and M. Rooks for their assistance and guidance in the device fabrication processes.

This research was sponsored by the Army Research Office (ARO) under grants no. W911NF-22-1-0053 and W911NF-23-1-0051, by DARPA under grant no. HR0011-24-2-0346, by the U.S. Department of Energy (DoE), Office of Science, National Quantum Information Science Research Centers, Co-design Center for Quantum Advantage (C2QA) under contract number DE-SC0012704, and by the Air Force Office of Scientific Research (AFOSR) under award number FA9550-21-1-0209. The views and conclusions contained in this document are those of the authors and should not be interpreted as representing the official policies, either expressed or implied, of the ARO, DARPA, DoE, AFOSR or the US Government. The US Government is authorized to reproduce and distribute reprints for Government purposes notwithstanding any copyright notation herein. Fabrication facilities use was supported by the Yale Institute for Nanoscience and Quantum Engineering (YINQE) and the Yale University Cleanroom. L.F. is a founder and shareholder of Quantum Circuits Inc. (QCI).

-
- [1] E. Dennis, A. Kitaev, A. Landahl, and J. Preskill, Topological quantum memory, *Journal of Mathematical Physics* **43**, 4452 (2002).
 - [2] A. Y. Kitaev, Fault-tolerant quantum computation by anyons, *Annals of Physics* **303**, 2 (2003).
 - [3] Google Quantum AI, [Quantum error correction below the surface code threshold](#) (2024), arXiv:2408.13687 [quant-ph].
 - [4] D. Sank, Z. Chen, and M. Khezri et al., Measurement-Induced State Transitions in a Superconducting Qubit: Beyond the Rotating Wave Approximation, *Physical Review Letters* **117**, 190503 (2016).
 - [5] M. Khezri and A. Opremcak et al., Measurement-induced state transitions in a superconducting qubit: Within the rotating-wave approximation, *Physical Review Applied* **20**, 054008 (2023).
 - [6] R. Shillito, A. Petrescu, J. Cohen, J. Beall, M. Hauru, M. Ganahl, A. G. Lewis, G. Vidal, and A. Blais, Dynamics of Transmon Ionization, *Physical Review Applied* **18**, 034031 (2022).
 - [7] X. Xiao, J. Venkatraman, R. G. Cortiñas, S. Chowdhury, and M. H. Devoret, [A diagrammatic method to compute the effective Hamiltonian of driven nonlinear oscillators](#) (2023), arXiv:2304.13656.
 - [8] J. Cohen, A. Petrescu, R. Shillito, and A. Blais, Reminiscence of Classical Chaos in Driven Transmons, *PRX Quantum* **4**, 020312 (2023).
 - [9] M. F. Dumas, B. Groleau-Paré, A. McDonald, M. H. Muñoz-Arias, C. Lledó, B. D’Anjou, and A. Blais, Measurement-Induced Transmon Ionization, *Physical Review X* **14**, 041023 (2024).
 - [10] K. N. Nesterov and I. V. Pechenezhskiy, Measurement-induced state transitions in dispersive qubit-readout schemes, *Physical Review Applied* **22**, 064038 (2024).
 - [11] A. Kitaev, Anyons in an exactly solved model and beyond, *Annals of Physics January Special Issue*, **321**, 2 (2006).
 - [12] M. A. Nielsen and I. L. Chuang, *Quantum Computation and Quantum Information: 10th Anniversary Edition* (2010), publisher: Cambridge University Press.
 - [13] L. Sun, L. DiCarlo, M. D. Reed, G. Catelani, L. S. Bishop, D. I. Schuster, B. R. Johnson, G. A. Yang, L. Frunzio, L. Glazman, M. H. Devoret, and R. J. Schoelkopf, Measurements of quasiparticle tunneling dynamics in a band-gap-engineered transmon qubit, *Physical Review Letters* **108**, 230509 (2012).
 - [14] N. Ofek, A. Petrenko, R. Heeres, P. Reinhold, Z. Leghtas, B. Vlastakis, Y. Liu, L. Frunzio, S. M. Girvin, L. Jiang, M. Mirrahimi, M. H. Devoret, and R. J. Schoelkopf, Extending the lifetime of a quantum bit with error correction in superconducting circuits, *Nature* **536**, 441 (2016).
 - [15] P. Campagne-Ibarcq, A. Eickbusch, S. Touzard, E. Zalys-Geller, N. E. Frattini, V. V. Sivak, P. Reinhold, S. Puri, S. Shankar, R. J. Schoelkopf, L. Frunzio, M. Mirrahimi, and M. H. Devoret, Quantum error correction of a qubit

- encoded in grid states of an oscillator, *Nature* **584**, 368 (2020).
- [16] V. V. Sivak, A. Eickbusch, B. Royer, S. Singh, I. Tsioutsios, S. Ganjam, A. Miano, B. L. Brock, A. Z. Ding, L. Frunzio, S. M. Girvin, R. J. Schoelkopf, and M. H. Devoret, Real-time quantum error correction beyond break-even, *Nature* **616**, 50 (2023).
- [17] Google Quantum AI, Suppressing quantum errors by scaling a surface code logical qubit, *Nature* **614**, 676 (2023).
- [18] V. B. Braginsky and F. Y. Khalili, Quantum nondemolition measurements: the route from toys to tools, *Reviews of Modern Physics* **68**, 1 (1996).
- [19] S. Moses, C. Baldwin, M. Allman, R. Ancona, L. Ascarunz, C. Barnes, J. Bartolotta, B. Bjork, P. Blanchard, M. Bohn, J. Bohnet, N. Brown, N. Burdick, W. Burton, S. Campbell, J. Campora, C. Carron, J. Chambers, J. Chan, Y. Chen, A. Chernoguzov, E. Chertkov, J. Colina, J. Curtis, R. Daniel, M. DeCross, D. Deen, C. Delaney, J. Dreiling, C. Ertsgaard, J. Esposito, B. Estey, M. Fabrikant, C. Figgatt, C. Foltz, M. Foss-Feig, D. Francois, J. Gaebler, T. Gatterman, C. Gilbreth, J. Giles, E. Glynn, A. Hall, A. Hankin, A. Hansen, D. Hayes, B. Higashi, I. Hoffman, B. Horning, J. Hout, R. Jacobs, J. Johansen, L. Jones, J. Karcz, T. Klein, P. Lauria, P. Lee, D. Liefer, S. Lu, D. Lucchetti, C. Lytle, A. Malm, M. Matheny, B. Mathewson, K. Mayer, D. Miller, M. Mills, B. Neyenhuis, L. Nugent, S. Olson, J. Parks, G. Price, Z. Price, M. Pugh, A. Ransford, A. Reed, C. Roman, M. Rowe, C. Ryan-Anderson, S. Sanders, J. Sedlacek, P. Shevchuk, P. Siegfried, T. Skripka, B. Spaun, R. Sprengle, R. Stutz, M. Swallows, R. Tobey, A. Tran, T. Tran, E. Vogt, C. Volin, J. Walker, A. Zolot, and J. Pino, A Race-Track Trapped-Ion Quantum Processor, *Physical Review X* **13**, 041052 (2023).
- [20] A. Paetznick, M. P. d. Silva, C. Ryan-Anderson, J. M. Bello-Rivas, J. P. C. III, A. Chernoguzov, J. M. Dreiling, C. Foltz, F. Frachon, J. P. Gaebler, T. M. Gatterman, L. Grans-Samuelsson, D. Gresh, D. Hayes, N. Hewitt, C. Holliman, C. V. Horst, J. Johansen, D. Lucchetti, Y. Matsuoka, M. Mills, S. A. Moses, B. Neyenhuis, A. Paz, J. Pino, P. Siegfried, A. Sundaram, D. Tom, S. J. Wernli, M. Zanner, R. P. Stutz, and K. M. Svore, *Demonstration of logical qubits and repeated error correction with better-than-physical error rates* (2024), arXiv:2404.02280 [quant-ph].
- [21] D. Bluvstein, S. J. Evered, A. A. Geim, S. H. Li, H. Zhou, T. Manovitz, S. Ebadi, M. Cain, M. Kalinowski, D. Hangleiter, J. P. Bonilla Ataides, N. Maskara, I. Cong, X. Gao, P. Sales Rodriguez, T. Karolyshyn, G. Semeghini, M. J. Gullans, M. Greiner, V. Vuletić, and M. D. Lukin, Logical quantum processor based on reconfigurable atom arrays, *Nature* **626**, 58 (2024).
- [22] R. Vijay, M. H. Devoret, and I. Siddiqi, Invited Review Article: The Josephson bifurcation amplifier, *Review of Scientific Instruments* **80**, 111101 (2009).
- [23] A. Roy and M. Devoret, Introduction to parametric amplification of quantum signals with Josephson circuits, *Comptes Rendus Physique Quantum microwaves / Micro-ondes quantiques*, **17**, 740 (2016).
- [24] J. Y. Mutus, T. C. White, R. Barends, Y. Chen, Z. Chen, B. Chiaro, A. Dunsworth, E. Jeffrey, J. Kelly, A. Megrant, C. Neill, P. J. J. O'Malley, P. Roushan, D. Sank, A. Vainsencher, J. Wenner, K. M. Sundqvist, A. N. Cleland, and J. M. Martinis, Strong environmental coupling in a Josephson parametric amplifier, *Applied Physics Letters* **104**, 263513 (2014).
- [25] C. Eichler, Y. Salathe, J. Mlynek, S. Schmidt, and A. Wallraff, Quantum-Limited Amplification and Entanglement in Coupled Nonlinear Resonators, *Physical Review Letters* **113**, 110502 (2014).
- [26] C. Macklin, K. O'Brien, D. Hover, M. E. Schwartz, V. Bolkhovskiy, X. Zhang, W. D. Oliver, and I. Siddiqi, A near-quantum-limited Josephson traveling-wave parametric amplifier, *Science* **350**, 307 (2015).
- [27] T. Roy, S. Kundu, M. Chand, A. M. Vadiraj, A. Ranadive, N. Nehra, M. P. Patankar, J. Aumentado, A. A. Clerk, and R. Vijay, Broadband parametric amplification with impedance engineering: Beyond the gain-bandwidth product, *Applied Physics Letters* **107**, 262601 (2015).
- [28] N. E. Frattini, V. V. Sivak, A. Lingenfelter, S. Shankar, and M. H. Devoret, Optimizing the nonlinearity and dissipation of a SNAIL parametric amplifier for dynamic range, *Physical Review Applied* **10**, 054020 (2018).
- [29] L. Planat, A. Ranadive, R. Dassonneville, J. Pueras Martínez, S. Léger, C. Naud, O. Buisson, W. Hasch-Guichard, D. M. Basko, and N. Roch, Photonic-Crystal Josephson Traveling-Wave Parametric Amplifier, *Physical Review X* **10**, 021021 (2020).
- [30] M. Esposito, A. Ranadive, L. Planat, and N. Roch, Perspective on traveling wave microwave parametric amplifiers, *Applied Physics Letters* **119**, 120501 (2021).
- [31] M. Malnou, M. Vissers, J. Wheeler, J. Aumentado, J. Hubmayr, J. Ullom, and J. Gao, Three-Wave Mixing Kinetic Inductance Traveling-Wave Amplifier with Near-Quantum-Limited Noise Performance, *PRX Quantum* **2**, 010302 (2021).
- [32] A. Blais, R.-S. Huang, A. Wallraff, S. M. Girvin, and R. J. Schoelkopf, Cavity quantum electrodynamics for superconducting electrical circuits: An architecture for quantum computation, *Physical Review A* **69**, 062320 (2004).
- [33] A. Wallraff, D. I. Schuster, A. Blais, L. Frunzio, R.-S. Huang, J. Majer, S. Kumar, S. M. Girvin, and R. J. Schoelkopf, Strong coupling of a single photon to a superconducting qubit using circuit quantum electrodynamics, *Nature* **431**, 162 (2004).
- [34] F. Mallet, F. R. Ong, A. Palacios-Laloy, F. Nguyen, P. Bertet, D. Vion, and D. Esteve, Single-shot qubit readout in circuit quantum electrodynamics, *Nature Physics* **5**, 791 (2009).
- [35] M. D. Reed, L. DiCarlo, B. R. Johnson, L. Sun, D. I. Schuster, L. Frunzio, and R. J. Schoelkopf, High-Fidelity Readout in Circuit Quantum Electrodynamics Using the Jaynes-Cummings Nonlinearity, *Physical Review Letters* **105**, 173601 (2010).
- [36] E. Jeffrey, D. Sank, J. Mutus, T. White, J. Kelly, R. Barends, Y. Chen, Z. Chen, B. Chiaro, A. Dunsworth, A. Megrant, P. O'Malley, C. Neill, P. Roushan, A. Vainsencher, J. Wenner, A. Cleland, and J. M. Martinis, Fast Accurate State Measurement with Superconducting Qubits, *Physical Review Letters* **112**, 190504 (2014).
- [37] T. Walter, P. Kurpiers, S. Gasparinetti, P. Magnard, A. Potočnik, Y. Salathé, M. Pechal, M. Mondal, M. Oppliger, C. Eichler, and A. Wallraff, Rapid High-Fidelity Single-Shot Dispersive Readout of Super-

- conducting Qubits, *Physical Review Applied* **7**, 054020 (2017).
- [38] R. Dassonneville, T. Ramos, V. Milchakov, L. Planat, E. Dumur, F. Foroughi, J. Puertas, S. Leger, K. Bhargava, J. Delaforce, C. Naud, W. Hasch-Guichard, J. Garcia-Ripoll, N. Roch, and O. Buisson, Fast High-Fidelity Quantum Nondemolition Qubit Readout via a Nonperturbative Cross-Kerr Coupling, *Physical Review X* **10**, 011045 (2020).
- [39] F. Swiadek, R. Shillito, P. Magnard, A. Remm, C. Hellings, N. Lacroix, Q. Ficheux, D. C. Zanuz, G. J. Norris, A. Blais, S. Krinner, and A. Wallraff, Enhancing Dispersive Readout of Superconducting Qubits through Dynamic Control of the Dispersive Shift: Experiment and Theory, *PRX Quantum* **5**, 040326 (2024).
- [40] P. A. Spring, L. Milanovic, Y. Sunada, S. Wang, A. F. van Loo, S. Tamate, and Y. Nakamura, Fast multiplexed superconducting qubit readout with intrinsic Purcell filtering (2024), arXiv:2409.04967 [quant-ph].
- [41] J. Gambetta, W. A. Braff, A. Wallraff, S. M. Girvin, and R. J. Schoelkopf, Protocols for optimal readout of qubits using a continuous quantum nondemolition measurement, *Physical Review A* **76**, 012325 (2007).
- [42] S. Hazra, W. Dai, T. Connolly, P. D. Kurilovich, Z. Wang, L. Frunzio, and M. H. Devoret, Benchmarking the readout of a superconducting qubit for repeated measurements (2024), arXiv:2407.10934.
- [43] J. Koch, T. M. Yu, J. Gambetta, A. A. Houck, D. I. Schuster, J. Majer, A. Blais, M. H. Devoret, S. M. Girvin, and R. J. Schoelkopf, Charge-insensitive qubit design derived from the Cooper pair box, *Physical Review A* **76**, 042319 (2007).
- [44] J. A. Schreier, A. A. Houck, J. Koch, D. I. Schuster, B. R. Johnson, J. M. Chow, J. M. Gambetta, J. Majer, L. Frunzio, M. H. Devoret, S. M. Girvin, and R. J. Schoelkopf, Suppressing charge noise decoherence in superconducting charge qubits, *Physical Review B* **77**, 180502 (2008).
- [45] P. Aliferis and B. M. Terhal, Fault-tolerant quantum computation for local leakage faults, *Quantum Info. Comput.* **7**, 139 (2007).
- [46] A. G. Fowler, Coping with qubit leakage in topological codes, *Physical Review A* **88**, 042308 (2013).
- [47] J. Ghosh, A. G. Fowler, J. M. Martinis, and M. R. Geller, Understanding the effects of leakage in superconducting quantum-error-detection circuits, *Physical Review A* **88**, 062329 (2013).
- [48] M. Suchara, A. W. Cross, and J. M. Gambetta, Leakage suppression in the Toric code, *Quantum Info. Comput.* **15**, 997 (2015).
- [49] P. Magnard, P. Kurpiers, B. Royer, T. Walter, J.-C. Besse, S. Gasparinetti, M. Pechal, J. Heinsoo, S. Storz, A. Blais, and A. Wallraff, Fast and Unconditional All-Microwave Reset of a Superconducting Qubit, *Physical Review Letters* **121**, 060502 (2018).
- [50] C. C. Bultink, T. E. O'Brien, R. Vollmer, N. Muthusubramanian, M. W. Beekman, M. A. Rol, X. Fu, B. Tarasinski, V. Ostroukh, B. Varbanov, A. Bruno, and L. DiCarlo, Protecting quantum entanglement from leakage and qubit errors via repetitive parity measurements, *Science Advances* **6**, eaay3050 (2020).
- [51] B. M. Varbanov, F. Battistel, B. M. Tarasinski, V. P. Ostroukh, T. E. O'Brien, L. DiCarlo, and B. M. Terhal, Leakage detection for a transmon-based surface code, *npj Quantum Information* **6**, 1 (2020).
- [52] M. McEwen et al., Removing leakage-induced correlated errors in superconducting quantum error correction, *Nature Communications* **12**, 1761 (2021).
- [53] K. C. Miao and M. McEwen et al., Overcoming leakage in quantum error correction, *Nature Physics* **19**, 1780 (2023).
- [54] T. Connolly and P. D. Kurilovich et al., In preparation.
- [55] See supplementary materials.
- [56] M. D. Reed, B. R. Johnson, A. A. Houck, L. DiCarlo, J. M. Chow, D. I. Schuster, L. Frunzio, and R. J. Schoelkopf, Fast reset and suppressing spontaneous emission of a superconducting qubit, *Applied Physics Letters* **96**, 203110 (2010).
- [57] A. V. Dixit, S. Chakram, K. He, A. Agrawal, R. K. Naik, D. I. Schuster, and A. Chou, Searching for Dark Matter with a Superconducting Qubit, *Physical Review Letters* **126**, 141302 (2021).
- [58] C. Braggio, L. Balembois, R. D. Vora, Z. Wang, J. Travesedo, L. Pallegoix, G. Carugno, A. Ortolan, G. Ruoso, U. Gambardella, D. D'Agostino, P. Bertet, and E. Flurin, Quantum-enhanced sensing of axion dark matter with a transmon-based single microwave photon counter (2024), arXiv:2403.02321 [quant-ph].
- [59] F. Zhao, Z. Li, A. V. Dixit, T. Roy, A. Vrajitoarea, R. Banerjee, A. Anferov, K.-H. Lee, D. I. Schuster, and A. Chou, A Flux-Tunable cavity for Dark matter detection (2025), arXiv:2501.06882 [quant-ph].
- [60] E. Albertinale, L. Balembois, E. Billaud, V. Ranjan, D. Flanigan, T. Schenkel, D. Estève, D. Vion, P. Bertet, and E. Flurin, Detecting spins by their fluorescence with a microwave photon counter, *Nature* **600**, 434 (2021).
- [61] Z. Wang, L. Balembois, M. Rančić, E. Billaud, M. Le Dantec, A. Ferrier, P. Goldner, S. Bertaina, T. Chanelière, D. Esteve, D. Vion, P. Bertet, and E. Flurin, Single-electron spin resonance detection by microwave photon counting, *Nature* **619**, 276 (2023).
- [62] J. O'Sullivan, J. Travesedo, L. Pallegoix, Z. W. Huang, A. May, B. Yavkin, P. Hogan, S. Lin, R. Liu, T. Chanelière, S. Bertaina, P. Goldner, D. Esteve, D. Vion, P. Abgrall, P. Bertet, and E. Flurin, Individual solid-state nuclear spin qubits with coherence exceeding seconds (2024), arXiv:2410.10432 [quant-ph].
- [63] L. Pallegoix, J. Travesedo, A. S. May, L. Balembois, D. Vion, P. Bertet, and E. Flurin, Enhancing the sensitivity of single microwave photon detection with bandwidth tunability (2025), arXiv:2501.07354 [quant-ph].
- [64] T. Larsen, K. Petersson, F. Kuemmeth, T. Jespersen, P. Krogstrup, J. Nygård, and C. Marcus, Semiconductor-Nanowire-Based Superconducting Qubit, *Physical Review Letters* **115**, 127001 (2015).
- [65] J. I.-J. Wang, D. Rodan-Legrain, L. Bretheau, D. L. Campbell, B. Kannan, D. Kim, M. Kjaergaard, P. Krantz, G. O. Samach, F. Yan, J. L. Yoder, K. Watanabe, T. Taniguchi, T. P. Orlando, S. Gustavsson, P. Jarillo-Herrero, and W. D. Oliver, Coherent control of a hybrid superconducting circuit made with graphene-based van der Waals heterostructures, *Nature Nanotechnology* **14**, 120 (2019).
- [66] H. Paik, A. Mezzacapo, M. Sandberg, D. McClure, B. Abdo, A. Córcoles, O. Dial, D. Bogorin, B. Plourde, M. Steffen, A. Cross, J. Gambetta, and J. M. Chow, Experimental Demonstration of a Resonator-Induced Phase Gate in a Multiqubit Circuit-QED System, *Physical Review Letters* **117**, 250502 (2016).

- [67] A. Eickbusch, V. Sivak, A. Z. Ding, S. S. Elder, S. R. Jha, J. Venkatraman, B. Royer, S. M. Girvin, R. J. Schoelkopf, and M. H. Devoret, Fast universal control of an oscillator with weak dispersive coupling to a qubit, *Nature Physics* **18**, 1464 (2022).
- [68] T. Oka and S. Kitamura, Floquet Engineering of Quantum Materials, *Annual Review of Condensed Matter Physics* **10**, 387 (2019).
- [69] M. F. Gely, G. A. Steele, and D. Bothner, Nature of the Lamb shift in weakly anharmonic atoms: From normal-mode splitting to quantum fluctuations, *Physical Review A* **98**, 053808 (2018).
- [70] This result is simplified by assuming the optimal resonator linewidth. General expression valid for arbitrary linewidth can be found in [84, 85].
- [71] The transition amplitude is determined by the charge operator because the readout resonator is coupled to the transmon capacitively. Undesired resonances would be also exponentially suppressed with inductive coupling.
- [72] This simulation disregards the measurement-induced dephasing present when the drive is delivered through a readout resonator. Accounting for this effect would broaden the resonant features in the plot, but their density would be unaffected.
- [73] Both the measurement rate and the Stark shift are proportional to $\chi\bar{n}$, where χ is the dispersive shift and \bar{n} is the number of photons in the readout resonator.
- [74] When designing the capacitor structures, we make sure that the frequencies of the associated spurious modes exceed 15 GHz.
- [75] E. M. Purcell, H. C. Torrey, and R. V. Pound, Resonance Absorption by Nuclear Magnetic Moments in a Solid, *Physical Review* **69**, 37 (1946).
- [76] D. Kleppner, Inhibited Spontaneous Emission, *Physical Review Letters* **47**, 233 (1981).
- [77] P. Goy, J. M. Raimond, M. Gross, and S. Haroche, Observation of Cavity-Enhanced Single-Atom Spontaneous Emission, *Physical Review Letters* **50**, 1903 (1983).
- [78] A. A. Houck, J. A. Schreier, B. R. Johnson, J. M. Chow, J. Koch, J. M. Gambetta, D. I. Schuster, L. Frunzio, M. H. Devoret, S. M. Girvin, and R. J. Schoelkopf, Controlling the Spontaneous Emission of a Superconducting Transmon Qubit, *Physical Review Letters* **101**, 080502 (2008).
- [79] A. Yen, Y. Ye, K. Peng, J. Wang, G. Cunningham, M. Gingras, B. M. Niedzielski, H. Stickler, K. Serniak, M. E. Schwartz, and K. P. O'Brien, Interferometric Purcell suppression of spontaneous emission in a superconducting qubit (2024), arXiv:2405.10107.
- [80] S. Touzard, A. Kou, N. Frattini, V. Sivak, S. Puri, A. Grimm, L. Frunzio, S. Shankar, and M. Devoret, Gated Conditional Displacement Readout of Superconducting Qubits, *Physical Review Letters* **122**, 080502 (2019).
- [81] D. McClure, H. Paik, L. Bishop, M. Steffen, J. M. Chow, and J. M. Gambetta, Rapid Driven Reset of a Qubit Readout Resonator, *Physical Review Applied* **5**, 011001 (2016).
- [82] Y. Sunada, S. Kono, J. Ilves, S. Tamate, T. Sugiyama, Y. Tabuchi, and Y. Nakamura, Fast Readout and Reset of a Superconducting Qubit Coupled to a Resonator with an Intrinsic Purcell Filter, *Physical Review Applied* **17**, 044016 (2022).
- [83] J.-H. Yeh, J. LeFebvre, S. Premaratne, F. C. Wellstood, and B. S. Palmer, Microwave attenuators for use with quantum devices below 100 mK, *Journal of Applied Physics* **121**, 224501 (2017).
- [84] J. Gambetta, A. Blais, D. I. Schuster, A. Wallraff, L. Frunzio, J. Majer, M. H. Devoret, S. M. Girvin, and R. J. Schoelkopf, Qubit-photon interactions in a cavity: Measurement-induced dephasing and number splitting, *Physical Review A* **74**, 042318 (2006).
- [85] A. A. Clerk, M. H. Devoret, S. M. Girvin, F. Marquardt, and R. J. Schoelkopf, Introduction to quantum noise, measurement, and amplification, *Reviews of Modern Physics* **82**, 1155 (2010).

Supplementary information for “High-frequency readout free of transmon multi-excitation resonances”

Pavel D. Kurilovich,^{1,*} Thomas Connolly,^{1,*} Charlotte G. L. Böttcher,^{1,†} Daniel K. Weiss,^{1,2,‡} Sumeru Hazra,¹ Vidul R. Joshi,^{1,§} Andy Z. Ding,¹ Heekun Nho,¹ Spencer Diamond,¹ Vladislav D. Kurilovich,^{1,¶} Wei Dai,¹ Valla Fatemi,^{1,3} Luigi Frunzio,¹ Leonid I. Glazman,^{1,2} and Michel H. Devoret^{1,**}

¹*Departments of Applied Physics and Physics, Yale University, New Haven, Connecticut 06520, USA*

²*Yale Quantum Institute, Yale University, New Haven, Connecticut 06511, USA*

³*School of Applied and Engineering Physics, Cornell University, Ithaca, New York 14853, USA*

(Dated: January 17, 2025)

CONTENTS

I. Experimental setup	2
A. Wiring diagram	2
B. Fabrication details	3
C. Packaging details	3
II. Purcell effect in high-frequency readout	3
III. Dispersive shift in high-frequency readout	5
A. Calculation of the dispersive shift	5
1. Corrections to the charge matrix elements	6
2. Final result for the dispersive shift	6
3. Reproducing the result for dispersive shift in the small detuning limit	7
B. Comparison to the experiment	7
C. Resonances in the dispersive shift	8
IV. Quantum non-demolition fidelity	8
A. Definition of QND fidelity	9
B. Comparison of QND fidelity to readout fidelity and repeatability	10
V. Details of QND fidelity measurement	10
A. Residual photon number	10
B. Leakage checks	11
C. Stability of the QND fidelity with time	11
VI. Details of Floquet simulations	12
A. Definition of Floquet modes through the propagator	12
B. Simple example of identifying resonances via Floquet modes	13
C. Using Floquet modes to identify resonances in a transmon qubit	13
D. Additional Floquet simulations	15
E. Comparison of transition amplitudes between simulation and simple analytical theory	15
References	16

* These two authors contributed equally.

pavel.kurilovich@yale.edu, tom.connolly@yale.edu

† Present address: Department of Applied Physics, Stanford University, Stanford, California 94305, USA

‡ Present address: Quantum Circuits, Inc., New Haven, CT, USA

§ Present address: Microsoft Quantum

¶ Present address: Google Quantum AI, 301 Mentor Dr, Goleta, CA93111, USA

** michel.devoret@yale.edu

Present address: Physics Dept., U.C. Santa Barbara, Santa Barbara, California 93106, USA and Google Quantum AI, 301 Mentor Dr, Goleta, California 93111, USA

I. EXPERIMENTAL SETUP

A. Wiring diagram

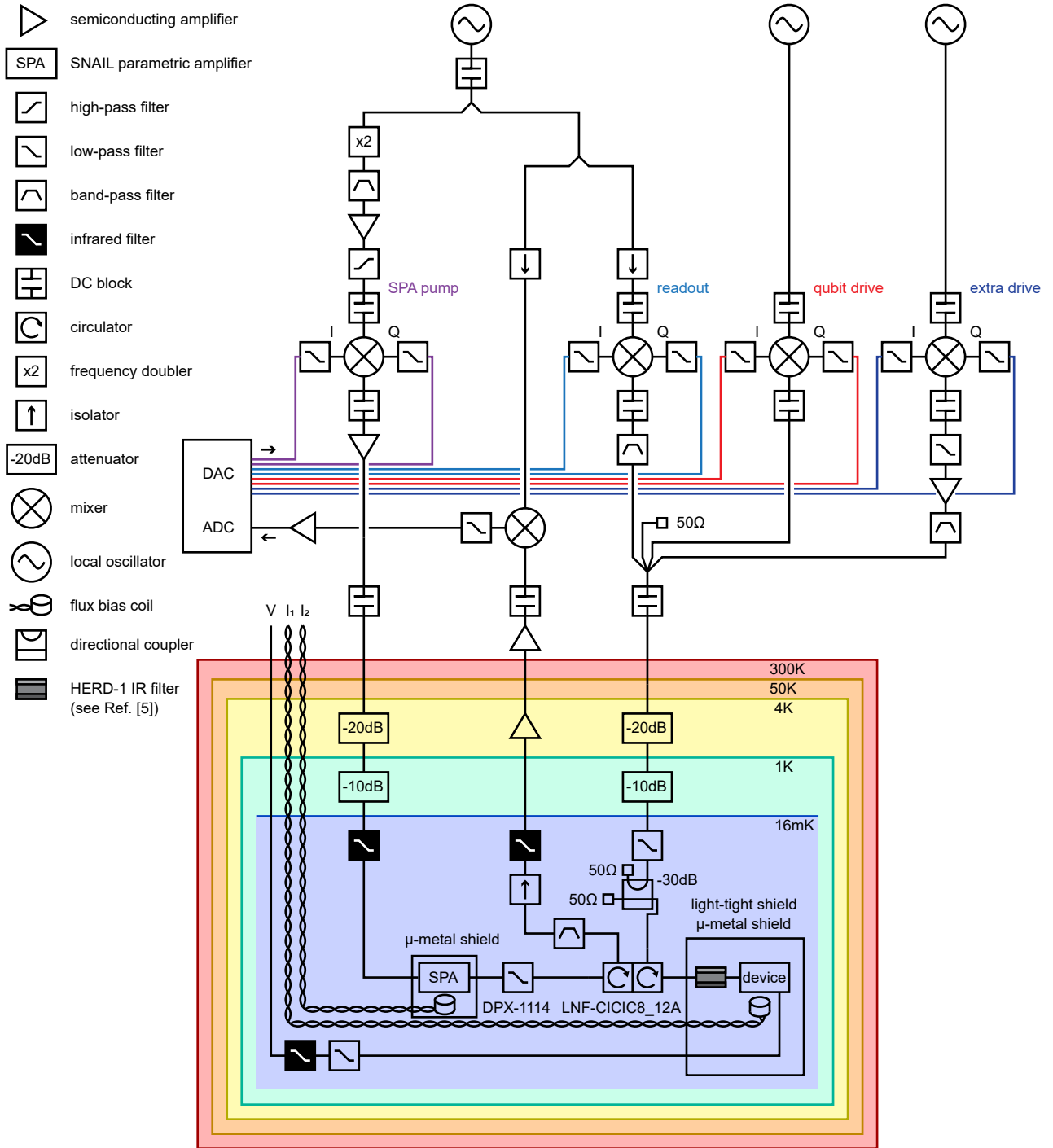


FIG. S1. Wiring diagram of the setup.

B. Fabrication details

Our transmon is fabricated on an annealed EFG Sapphire substrate. The transmon Josephson junction is an Al/AlOx/Al trilayer made using the bridge-free technique. The transmon pads, readout resonator, and ground plane are made of tantalum. This was shown to improve the quality factor compared to an all-aluminum transmon fabrication [1, 2]. The Al/AlOx/Al junctions and the tantalum structures are demonstrated in Figure S2(a).

The fabrication of the tantalum layer follows Ref. [2]. The bridge-free Josephson junction fabrication is similar to that described in Ref. [3] except for two nuances. First, when forming the Josephson junction, we oxidized the aluminum film at a higher pressure of 50 Torr for a longer duration of 30 minutes. This allowed us to substantially lower the Josephson energy compared to Ref. [3] without reducing the junction size. Second, compared to Ref. [3] we used more aggressive ion milling in order to make a good contact between tantalum and aluminum. Ion milling was similar to that employed in Ref. [2].

C. Packaging details

The 7 mm by 7 mm chip hosting the transmon was placed in a copper package. To reduce the participation of lossy copper in the device and to increase the frequency of spurious box modes, we carved an air-gap below and above the chip. The schematic of the package is shown in Figure S2(b). The package is then embedded in an additional light-tight shield which protects it from stray infrared radiation; this suppresses the qubit heating and reduces quasiparticle-related decoherence. The shield is analogous to that described in Ref. [4]. Inside the shield, we used a low-loss HERD-1 low-pass filter [5] to suppress the infrared radiation coming from the readout line. We use small dots of silver paste at the corners of the sapphire chip to thermalize it to the copper package.

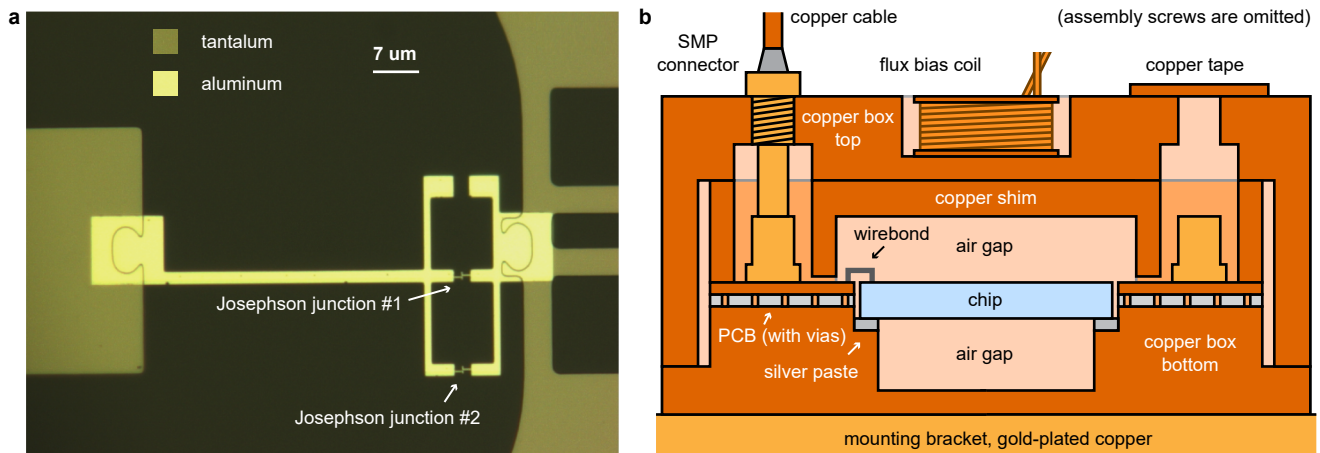


FIG. S2. Chip and packaging details. (a) Zoom in on the Josephson junction region of our device. Al/AlOx/Al superconducting quantum interference device (SQUID) is interfaced with the tantalum pads and the ground plane. The on-chip flux lines (on the right from the SQUID) and an additional SQUID arm are not used in the present experiment. The flux lines are shorted to the ground plane with wirebonds and the extra SQUID arm is left open. (b) Schematic of the package hosting the chip (scale not preserved).

II. PURCELL EFFECT IN HIGH-FREQUENCY READOUT

The transmon inherits dissipation through its capacitive coupling to a lossy readout resonator. This is known as the Purcell effect [6–8]; it places a limit on the coherence time of the qubit. In this section, we analyze the Purcell effect in the limit where the frequency of the readout resonator vastly exceeds that of the transmon, $\omega_r \gg \omega_q$. We show that the Purcell effect becomes suppressed by ω_r/ω_q raised to a high power, compared to the well-know expression [9, 10] derived for the case $|\omega_r - \omega_q| \ll \omega_q$. The degree of suppression depends on whether the coupling between the resonator and the transmission line is capacitive or inductive; we consider both cases here. Throughout the derivation we neglect direct coupling between the transmon and the transmission line. We also assume that the impedance of a transmission line is independent of frequency.

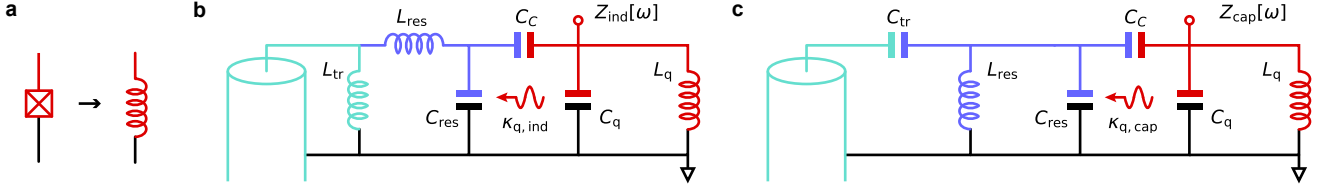


FIG. S3. Schematics of the lumped-element circuits used to estimate the Purcell decay rate for the high-frequency readout. (a) To estimate the Purcell decay rate, we use classical circuit analysis. To this end, we replace the Josephson junction with a linear inductor. (b) Notations of circuit elements in the case when the readout resonator is inductively coupled to the transmission line. This lumped circuit can be used to model a $\lambda/4$ readout resonator used in our manuscript. (c) Same for the case of a resonator capacitively coupled to the transmission line.

To describe the Purcell effect, we resort to classical circuit analysis. To this end, we replace the Josephson junction of our transmon with a linear inductance. The resulting lumped model of our device is shown in Fig. S3. The parameters of this model can be constrained by the measured qubit and resonator frequencies. Assuming that the coupling between the resonator and the transmission line is weak, we obtain

$$\omega_r^2 = \frac{C_q + C_C}{L_{res}C_\Sigma^2}, \quad \omega_q^2 = \frac{1}{L_q(C_q + C_C)}, \quad C_\Sigma^2 = C_{res}C_q + C_{res}C_C + C_qC_C. \quad (S1)$$

In deriving these equations, we assumed $\omega_r \gg \omega_q$ and thus neglected corrections of order $\eta^2(\omega_q/\omega_r)^2$, where coupling efficiency $0 < \eta < 1$ is defined¹ as

$$\eta = \frac{C_C}{\sqrt{(C_{res} + C_C)(C_q + C_C)}}. \quad (S2)$$

Qualitatively, neglecting these corrections amounts to replacing the qubit inductance with an open at $\omega = \omega_r$ and resonator inductance with a short at $\omega = \omega_q$.

We begin by finding the resonator linewidth in terms of the circuit parameters of Fig. S3. For the inductive and capacitive coupling between the resonator and the transmission line we find respectively

$$\kappa_{ind} = \frac{L_{tr}^2 \omega_r^2}{Z_0 L_{res}}, \quad \kappa_{cap} = \frac{\omega_r^2 Z_0 C_{tr}^2 (C_q + C_C)}{C_\Sigma^2}. \quad (S3)$$

Here, Z_0 is the characteristic impedance of the transmission line. Next, we find the qubit linewidth – which quantifies the dissipation due to the Purcell effect – by evaluating the impedance of the island close to the qubit frequency ($|\omega - \omega_q| \ll \omega_q$). Explicitly, for the two cases we find

$$Z_{ind}[\omega] = \frac{1}{\frac{1}{i\omega L_q} + i\omega(C_q + C_C) + \frac{\omega^4 C_C^2 L_{tr}^2}{Z_0}}, \quad Z_{cap}[\omega] = \frac{1}{\frac{1}{i\omega L_q} + i\omega(C_q + C_C) + \omega^6 C_C^2 C_{tr}^2 L_{res}^2 Z_0} \quad (S4)$$

Correspondingly, we obtain the qubit linewidth in both cases

$$\kappa_{q,ind} = \frac{\eta^2}{1 - \eta^2} \frac{\omega_q^4}{\omega_r^4} \kappa_{ind}, \quad \kappa_{q,cap} = \frac{\eta^2}{1 - \eta^2} \frac{\omega_q^6}{\omega_r^6} \kappa_{cap}. \quad (S5)$$

Alternatively, we can rewrite these equations in term of the coupling strength $g = \frac{1}{2}\eta\sqrt{\omega_q\omega_r}$:

$$\kappa_{q,ind} = \frac{1}{1 - \eta^2} \frac{4\omega_q^3}{\omega_r^3} \frac{g^2}{\omega_r^2} \kappa_{ind}, \quad \kappa_{q,cap} = \frac{1}{1 - \eta^2} \frac{4\omega_q^5}{\omega_r^5} \frac{g^2}{\omega_r^2} \kappa_{cap}. \quad (S6)$$

Notably, these equations are different from a standard expression for the Purcell effect [9, 10] derived under the assumptions $|\omega_r - \omega_q| \ll \omega_q$ and $\eta^2 \ll 1$,

$$\kappa_q = \frac{g^2}{(\omega_r - \omega_q)^2} \kappa. \quad (S7)$$

¹ We implicitly assumed that η is sufficiently far from unity. The case $1 - \eta \ll 1$ should be treated separately, and is outside of the scope of our work.

Compared to this expression, Purcell decay is suppressed by multiple powers of the large parameter ω_r/ω_q . This suppression arises from the frequency dependence of the impedance of the coupling elements. For example, capacitive coupling between the resonator and the transmission line becomes shunted by the resonator inductance at small frequencies. Additionally, linewidths in Eq. (S6) contain an extra prefactor of $1/(1 - \eta^2)$ compared to Eq. (S7). In the main text of the manuscript we assumed $\eta^2 \ll 1$ and thus neglected this prefactor. We note that deviations from the standard formula for the Purcell effect have been recently discussed in Ref. [11].

III. DISPERSIVE SHIFT IN HIGH-FREQUENCY READOUT

In this section, we derive the expressions for the frequency pull of the readout resonator induced by its capacitive coupling to the transmon qubit. The frequency pull depends on the transmon state. We denote the frequency pull when the transmon is in its n -th excited state as χ_n . The difference in resonator frequency when the qubit is in its ground state and its first excited state $\chi = \chi_1 - \chi_0$, known as the dispersive shift, allows us to perform qubit measurements.

The resulting formula for χ that we obtain is different from the well-known result valid for $|\omega_r - \omega_q| \ll \omega_q$ [12]. The difference arises due to the inclusion of counter-rotating terms in the coupling Hamiltonian, which become important when $\omega_r/\omega_q \gg 1$. We show how accounting for the counter-rotating terms enhances the dispersive shift compared to the standard readout regime. We compare the measured dispersive shifts to our formula and find excellent agreement. Throughout this section, we assume that the Josephson energy E_J vastly exceeds the charging energy E_C , such that the circuit is deep in the transmon regime.

A. Calculation of the dispersive shift

The Hamiltonian of a transmon coupled to a readout resonator is given by

$$H = 4E_C(N - n_g)^2 - E_J \cos \varphi + \hbar g \frac{N}{N_{\text{zpf}}} (a + a^\dagger) + \hbar \omega_{r,\text{bare}} (a^\dagger a + 1/2). \quad (\text{S8})$$

Here N is the operator of the number of Cooper pairs on the transmon island and φ is the canonically conjugate superconducting phase operator. The parameter $N_{\text{zpf}} = (E_J/32E_C)^{1/4}$ denotes the zero point fluctuations of the transmon charge. The readout resonator has bare frequency $\omega_{r,\text{bare}}$; the corresponding creation and annihilation operators are a^\dagger and a , respectively. Parameter g denotes the coupling strength between the readout resonator and the transmon.

The bare resonator frequency $\omega_{r,\text{bare}}$ does not account for the presence of the Josephson junction; it would be the resonator frequency if the Josephson junction was replaced by an open circuit. We can compute corrections to this bare frequency due to the presence of the junction using second-order perturbation theory. When the transmon is in its n -th excited state, $|n\rangle$, the frequency shift of the resonator χ_n is [3, 13, 14]

$$\hbar \chi_n = \frac{(\hbar g)^2}{N_{\text{zpf}}^2} \sum_{m \neq n} |\langle n|N|m\rangle|^2 \frac{2E_{nm}}{E_{nm}^2 - (\hbar \omega_{r,\text{bare}})^2}. \quad (\text{S9})$$

Here, $E_{nm} = E_n - E_m$, with E_n the energy of the n -th excited transmon state (for computational states $n = 0, 1$). In the high-frequency readout regime, we can safely restrict the summation to $m = n \pm 1$ as long as $E_J \gg E_C$. One concern with this restriction is the contribution of terms with $|E_{nm}|$ close to $\hbar \omega_{r,\text{bare}}$, corresponding to multi-excitation resonances. For these terms with $m \neq n \pm 1$, the denominator in Eq. (S9) becomes small. The matrix element for the corresponding transitions is, however, exponentially small in the ratio $\omega_{r,\text{bare}}/\omega_q$, as explained in the main text. This justifies restricting the summations $m = n \pm 1$ for a sufficiently large $\omega_{r,\text{bare}}/\omega_q$. We analyze the case when these transitions become important in Section III C.

For the transmon in the ground state, the resonator frequency shift is given by

$$\hbar \chi_0 = \frac{(\hbar g)^2}{N_{\text{zpf}}^2} |\langle 0|N|1\rangle|^2 \frac{2E_{10}}{(\hbar \omega_{r,\text{bare}})^2 - E_{10}^2}. \quad (\text{S10})$$

Here, the matrix element $|\langle 0|N|1\rangle|^2$ is close to N_{zpf}^2 in the transmon regime. As we explain below, however, it is important to go beyond this approximation when computing the difference between χ_1 and χ_0 .

For the transmon in the first excited state, the resonator frequency shift is

$$\hbar\chi_1 = -\frac{(\hbar g)^2}{N_{\text{zpf}}^2} |\langle 0|N|1\rangle|^2 \frac{2E_{10}}{(\hbar\omega_{\text{r,bare}})^2 - E_{10}^2} + \frac{(\hbar g)^2}{N_{\text{zpf}}^2} |\langle 1|N|2\rangle|^2 \frac{2E_{21}}{(\hbar\omega_{\text{r,bare}})^2 - E_{21}^2}. \quad (\text{S11})$$

The dispersive shift, quantity most relevant for qubit readout, is defined as $\hbar\chi = \hbar\chi_1 - \hbar\chi_0$. We find

$$\hbar\chi = 2\frac{(\hbar g)^2}{N_{\text{zpf}}^2} \left(|\langle 1|N|2\rangle|^2 \frac{E_{21}}{(\hbar\omega_{\text{r,bare}})^2 - E_{21}^2} - |\langle 0|N|1\rangle|^2 \frac{2E_{10}}{(\hbar\omega_{\text{r,bare}})^2 - E_{10}^2} \right) \quad (\text{S12})$$

1. Corrections to the charge matrix elements

To further simplify expression (S12), care is needed when evaluating the matrix elements of N . To get a valid expression for χ , it is essential to account for the corrections to these matrix elements due to the transmon non-linearity. As we explain below, taking these corrections into the account results in

$$|\langle 1|N|2\rangle|^2 = 2|\langle 1|N|0\rangle|^2 \left(1 - \frac{E_C}{E_{10}} \right) = 2|\langle 1|N|0\rangle|^2 \frac{E_{21}}{E_{10}}. \quad (\text{S13})$$

The simplifying assumption $|\langle 1|N|2\rangle|^2 = 2|\langle 0|N|1\rangle|^2$ would lead to an incorrect result for the dispersive shift. This occurs because in the leading approximation in E_C the dispersive shift vanishes in Eq. (S12). It is then necessary to keep track of corrections linear in E_C .

To derive Eq. (S13), one can approximate the transmon Hamiltonian with that of a non-linear oscillator with a quartic nonlinearity. This is achieved by replacing $N = N_{\text{zpf}}(b + b^\dagger)$, $\varphi = -i\varphi_{\text{zpf}}(b - b^\dagger)$, and expanding the cosine potential of the transmon to the fourth order. Here, zero point fluctuations of the phase, φ_{zpf} , are related to that of the charge via $\varphi_{\text{zpf}}N_{\text{zpf}} = 1/2$. The resulting Hamiltonian reads

$$H_{\text{tr}} = H_0 + V, \quad H_0 = \hbar\omega_q(b^\dagger b + 1/2), \quad V = -\frac{E_C}{12}(b - b^\dagger)^4. \quad (\text{S14})$$

Here, we treat V as a perturbation. To compute the matrix element $|\langle i|N|i+1\rangle|^2$, we expand transmon eigenstates $|i\rangle$ and $|i+1\rangle$ into the eigenstates of H_0 up to the first order in V . This way, we find

$$|i\rangle = |i\rangle_0 - \frac{E_C}{24\hbar\omega_q}(4i+6)\sqrt{i+1}\sqrt{i+2}|i+2\rangle_0 + \dots, \quad (\text{S15})$$

$$|i+1\rangle = |i+1\rangle_0 + (4i+2)\frac{E_C}{24\hbar\omega_q}\sqrt{i+1}\sqrt{i}|i-1\rangle_0 + \dots. \quad (\text{S16})$$

Here, “0” subscript indicates the eigenstates of H_0 and ... denote terms irrelevant for the calculation of $|\langle i|N|i+1\rangle|^2$. Substituting Eq. (S15) and Eq. (S16) into the matrix element in question, we find

$$|\langle i|N|i+1\rangle|^2 = (i+1)N_{\text{zpf}}^2 \left(1 - \frac{E_C}{\hbar\omega_q}(i+1) \right), \quad (\text{S17})$$

which results in Eq. (S13).

2. Final result for the dispersive shift

Substituting Eq. (S13) into Eq. (S12), we obtain

$$\hbar\chi = -8E_C \frac{(\hbar g)^2(\hbar\omega_{\text{r,bare}})^2}{[(\hbar\omega_{\text{r,bare}})^2 - E_{10}^2][(\hbar\omega_{\text{r,bare}})^2 - E_{21}^2]} \quad (\text{S18})$$

Neglecting the qubit energies E_{10} and E_{21} in the denominators and also neglecting the distinction between ω_r and $\omega_{\text{r,bare}}$, we retrieve $\hbar\chi = -8E_C g^2/\omega_r^2$, formula presented in the main text. We note that equation (S18) can be alternatively derived using the formalism of Ref. [15]. An equation analogous to Eq. (S18) was also derived in Ref. [16] via normal mode decomposition. In contrast to our approach, the approach of Ref. [16] neglects the difference between $\omega_q = E_{10}/\hbar$ and E_{21}/\hbar .

As long as $\omega_{r,\text{bare}} \gg \omega_q$, cavity pulls in higher transmon states can be approximated as $\chi_n = \chi_0 - n\chi$ for states within the Josephson well, $E_n < E_J$. The equation (S10) for the cavity pull χ_0 also simplifies in the case of high-frequency readout. Namely, for $\omega_{r,\text{bare}} \gg \omega_q$ we obtain

$$\chi_0 = 2\omega_q \frac{g^2}{\omega_r^2}. \quad (\text{S19})$$

We note that in the validity regime of perturbation theory, $g \ll \omega_r$, cavity pull satisfies $\chi_0 \ll \omega_q \ll \omega_r$. For the parameters used in the main text we obtain $\chi_0/2\pi = 4.7$ MHz. For this reason, in the main text and in Section II, we do not draw a distinction between ω_r and $\omega_{r,\text{bare}}$

3. Reproducing the result for dispersive shift in the small detuning limit

We note that Eq. (S18) also correctly describes the dispersive shift in the regime $|\omega_{r,\text{bare}} - \omega_q| \ll \omega_q$ (in addition to the regime $\omega_{r,\text{bare}} \gg \omega_q$). Indeed, in this regime the summation in Eq. (S9) can also be restricted to $m = n \pm 1$ which was the only assumption in our derivation. To see that this is case, we note that in the small detuning regime we can approximate

$$\begin{aligned} \chi &= -8E_C \frac{(\hbar g)^2 (\hbar\omega_{r,\text{bare}})^2}{(E_{10} - \hbar\omega_{r,\text{bare}})(E_{21} - \hbar\omega_{r,\text{bare}})(E_{10} + \hbar\omega_{r,\text{bare}})(E_{21} + \hbar\omega_{r,\text{bare}})} \approx \\ &\approx -8E_C \frac{(\hbar g)^2 (\hbar\omega_{r,\text{bare}})^2}{(E_{10} - \hbar\omega_{r,\text{bare}})(E_{21} - \hbar\omega_{r,\text{bare}}) \cdot 2\hbar\omega_{r,\text{bare}} \cdot 2\hbar\omega_{r,\text{bare}}} = \\ &= -2E_C \frac{(\hbar g)^2}{(\hbar\omega_{r,\text{bare}} - E_{10})(\hbar\omega_{r,\text{bare}} - E_{21})} = -2E_C \frac{g^2}{\Delta(\Delta - E_C/\hbar)}. \end{aligned} \quad (\text{S20})$$

Here, we introduced the conventional notation $\Delta = \omega_q - \omega_{r,\text{bare}}$. Eq. (S20) coincides with the established result of Ref. [12].

B. Comparison to the experiment

We experimentally measure the resonator frequencies for the qubit initialized in its different states. To this end, we send a short measurement pulse to the readout resonator and record the phase of the reflected signal. After collecting sufficient statistics, we change the frequency of the pulse and observe how the phase changes. As long as the transmon is kept in state $|n\rangle$, the phase winds by 2π around the shifted resonator frequency $\omega_n = \omega_{r,\text{bare}} + \chi_n$ (where $\omega_{r,\text{bare}}$ is the frequency of the resonator not dressed by its coupling to the qubit) as the probe frequency is changed. Finding the center of such a “phase-roll”, we extract ω_n . In practice, we do not actively keep the transmon in a given state. Rather, we rely on thermal fluctuations to populate the higher transmon states. As a result, with enough statistics, we can simultaneously observe phase-rolls corresponding to different transmon states and extract the resulting frequencies ω_n . We repeat this experiment at different values of the transmon Josephson energy, which we control by threading the magnetic flux through the SQUID loop of our device. The resulting dependence of the resonator frequencies ω_n on flux bias is shown in Figure S4.

Theoretically, the dependence of frequencies ω_0 and ω_1 on the flux bias stems from two contributions. First, qubit frequency ω_q in Eqs. (S18) and (S19) changes with flux. Second, the coupling strength g changes with flux. Indeed, in terms of the circuit parameters of Figure S3, the coupling strength can be expressed as

$$g = \frac{1}{2}\eta\sqrt{\omega_q\omega_{r,\text{bare}}}, \quad (\text{S21})$$

where parameter η is defined in Eq. (S2). Therefore, the flux dependence of g is also contained in the qubit frequency ω_q . We take both of the described contributions into the account when computing the frequencies ω_0 and ω_1 .

We compare the observed flux bias dependence of ω_0 and ω_1 to that predicted by Eqs. (S18) and (S19). To this end, we simultaneously fit the measured resonator frequencies to $\omega_0 = \omega_{r,\text{bare}} + \chi_0$ and $\omega_1 = \omega_{r,\text{bare}} + \chi_1$ using $\omega_{r,\text{bare}}$ and η as fitting parameters. We find that the theory is in the excellent agreement with the data both for ω_0 and for ω_1 . From this measurement we extract $\omega_{\text{bare}}/2\pi = 9.2233$ GHz and $\eta = 0.38$.

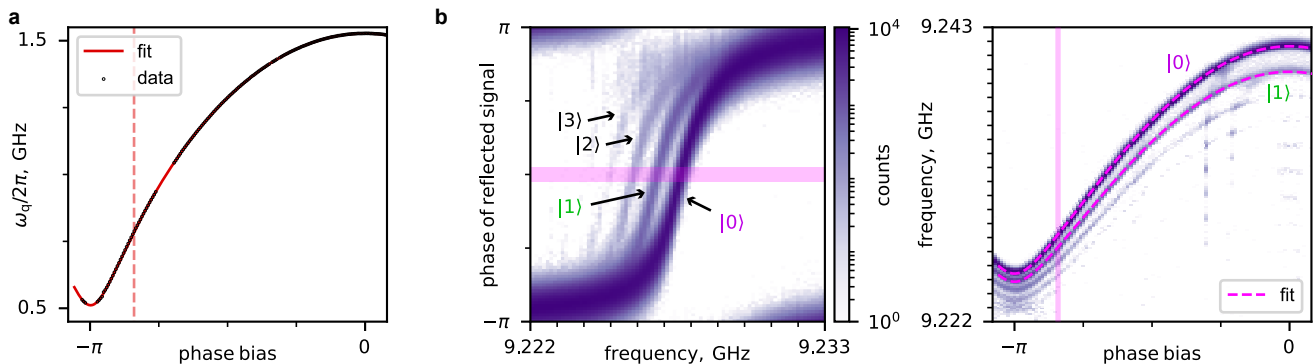


FIG. S4. Qubit and resonator spectroscopy. (a) Frequency of the $|0\rangle \rightarrow |1\rangle$ transition of our transmon as a function of SQUID phase bias. The red vertical line corresponds to the operation point considered in the main text of the manuscript. (b) Single-tone spectroscopy of the readout resonator. Left panel: histogram of the phase of the signal reflected from the resonator as a function of signal frequency. Different phase-rolls correspond to different transmon states (measurement is performed in a single-shot readout regime). The middle of each phase-roll indicates the resonator frequency for the corresponding transmon state. Right panel: resulting dependence of dispersive shifts on the phase bias. The theory fit is produced using Eqs. (S10) and (S18). Purple vertical line – operation point of the main text.

C. Resonances in the dispersive shift

Next, we analyze how well Eq. (S18) describes the dispersive shift for an arbitrary resonator frequency. To this end, we compare Eq. (S18) to the full expression Eq. (S9), in which we do not restrict the summation to terms with $n = m \pm 1$. The results of this comparison are presented in Figure S5, where we plot the dispersive shift as a function of the detuning between the readout resonator and the transmon. For visualization purposes, we normalize the dispersive shift by the conventional formula of Ref. [12] derived for the case $|\omega_{r,\text{bare}} - \omega_q| \ll \omega_q$,

$$\hbar\chi_{\text{RWA}} = -2E_C \frac{g^2}{\Delta(\Delta - E_C/\hbar)}, \quad \Delta = \omega_q - \omega_{r,\text{bare}}. \quad (\text{S22})$$

From the figure, it is apparent that Eq. (S18) correctly captures the dispersive shift both in the small-detuning regime, $|\omega_{r,\text{bare}} - \omega_q| \ll \omega_q$, and in the high-frequency readout regime², $\omega_{r,\text{bare}}/\omega_q \gg 1$. However, in the intermediate frequency regime, $|\omega_{r,\text{bare}} - \omega_q| \gtrsim \omega_q$, the approximate equation (S18) no longer holds. In this regime the summation in Eq. (S9) cannot be truncated to terms with $n = m \pm 1$ since transitions to higher transmon states might come into resonance with the readout frequency. The dispersive shift goes through a sequence of divergences as the readout frequency is increased. These resonances might lead to undesired readout-induced state transitions. Thus, we expect the performance of dispersive readout to be poor in the regime $|\omega_{r,\text{bare}} - \omega_q| \gtrsim \omega_q$. Only when $\omega_{r,\text{bare}}/\omega_q \gg 1$ do the multi-excitation resonances vanish exponentially, leading to the improved performance of the dispersive readout demonstrated in the main text.

As is also evident from the figure, the standard result of Ref. [12] correctly predicts the dispersive shift when $|\omega_q - \omega_{r,\text{bare}}| \ll \omega_q$. It fails, however, to capture the behavior of the dispersive shift outside of this regime. At high readout frequencies, it is essential to take into the account the counter-rotating terms in the coupling between the transmon and the resonator; these terms are neglected in Eq. (S22). When $\omega_{r,\text{bare}} \gg \omega_q$, counter-rotating terms enhance the dispersive shift roughly by a factor of four compared to the small detuning regime (for the same ratio between the coupling strength and detuning).

IV. QUANTUM NON-DEMOLITION FIDELITY

In this section, we elaborate on the definition of quantum non-demolition (QND) fidelity used in the main text of the manuscript. Notably, this metric of readout performance is different from other commonly used metrics: readout

² He we tacitly assume that the coupling between the resonator and the transmon is weak enough such that the perturbative treatment in the derivation of the dispersive shift is valid.

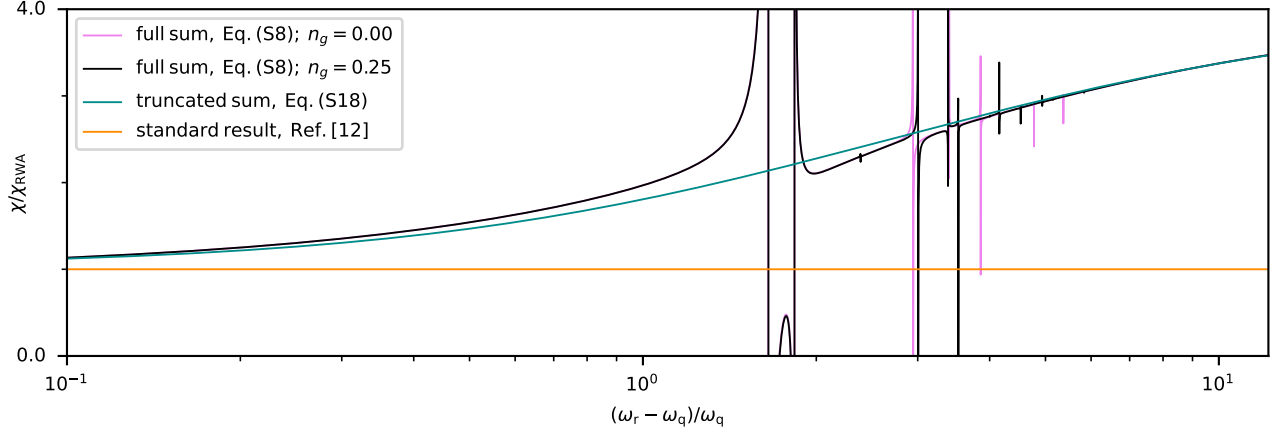


FIG. S5. Dispersive shift computed via the second order perturbation theory in transmon-resonator coupling strength as a function of detuning. Black and magenta solid lines show the results of Eq. (S9) for the offset charge $n_g = 0.25$ and $n_g = 0.00$, respectively. For simplicity of presentation, the curve is normalized by the “standard” formula for the dispersive shift, Eq. (S22), evaluated for the same values of parameters. Green solid line corresponds to a simplified expression for the dispersive shift, Eq. (S18). In contrast to a full perturbative result given by Eq. (S9), Eq. (S18) neglects terms in which state of the transmon (virtually) changes by more than one excitation. This approximation is justified both in the small detuning regime, $|\omega_{r,\text{bare}} - \omega_q| \ll \omega_q$, and in the large detuning regime, $\omega_{r,\text{bare}}/\omega_q \gg 1$. However, in the intermediate frequency range, $|\omega_{r,\text{bare}} - \omega_q| \gtrsim \omega_q$, the dispersive shift goes through a sequence of resonances. More resonances will appear if we go to higher order in perturbation theory. As explained in the main text, the resonances become exponentially suppressed in the regime $\omega_{r,\text{bare}}/\omega_q \gg 1$.

fidelity and “repeatability”. As we elaborate on below, the latter metrics do not faithfully account for leakage errors, i.e., transmon excitation to non-computational states [17]. They are thus not suitable for describing the readout performance for applications sensitive to leakage such as quantum error correction.

A. Definition of QND fidelity

We begin by rigorously defining the error probabilities $\varepsilon_{\text{assign}}$ and $\varepsilon_{\text{trans}}$ discussed in the main text. To this end, we introduce the quantity $P(i_s, j_m | k_s)$ where k_s to the right of the separating line stands for the prepared state $|k_s\rangle$; to the left of the separating line, j_m stands for the measurement result and i_s stands for the post-readout state $|i_s\rangle$. As such $P(i_s, j_m | k_s)$ is the probability that the measurement outcome is j_m and that the post-readout state is $|i_s\rangle$ conditioned on system being prepared in state $|k_s\rangle$ before the readout.

We introduce the QND fidelity as

$$\mathcal{Q} = \frac{1}{2} [P(1_s, 1_m | 1_s) + P(0_s, 0_m | 0_s)]. \quad (\text{S23})$$

The conditional probabilities in this definition can be decomposed as

$$P(i_s, i_m | i_s) = 1 - \sum_{j_s \neq i_s} P(j_s | i_s) - \sum_{j_m \neq i_s} P(i_s, j_m | i_s). \quad (\text{S24})$$

Here, $P(j_s | i_s)$ is the probability that the state after the readout is $|j_s\rangle$ given that the state before the readout is $|i_s\rangle$ (regardless of measurement outcome). Therefore, the first sum in Eq. (S24) describes the total probability of a *transition* error. In the same equation, $P(i_s, j_m | i_s)$ with $j_m \neq i_s$ is the probability that the readout did not change the state but the state was assigned erroneously. The second sum in Eq. (S24) thus describes the total probability of an *assignment* error. We define $\varepsilon_{\text{trans}}$ and $\varepsilon_{\text{assign}}$ as probabilities of transition and assignment errors, respectively, averaged over the computational states,

$$\varepsilon_{\text{trans}} = \frac{1}{2} \left[\sum_{j_s \neq 0_s} P(j_s | 0_s) + \sum_{j_s \neq 1_s} P(j_s | 1_s) \right] \quad \varepsilon_{\text{assign}} = \frac{1}{2} \left[\sum_{j_m \neq 0_s} P(0_s, j_m | 0_s) + \sum_{j_m \neq 1_s} P(1_s, j_m | 1_s) \right]. \quad (\text{S25})$$

We can further break down the transition error probability into the bit flip and leakage probabilities, $\varepsilon_{\text{trans}} = \varepsilon_{\text{trans}}^{\text{bit-flip}} + \varepsilon_{\text{trans}}^{\text{leakage}}$, where

$$\varepsilon_{\text{trans}}^{\text{bit-flip}} = \frac{1}{2} [P(1_s|0_s) + P(0_s|1_s)], \quad \varepsilon_{\text{trans}}^{\text{leakage}} = \frac{1}{2} \sum_{j_s > 1} [P(j_s|0_s) + P(j_s|1_s)]. \quad (\text{S26})$$

B. Comparison of QND fidelity to readout fidelity and repeatability

A more conventional definition of the readout fidelity is

$$\mathcal{F} = \frac{1}{2} [P(0_m|0_s) + P(1_m|1_s)], \quad (\text{S27})$$

where $P(i_m|i_s)$ is the probability of the readout outcome to be i_m if system was prepared in state $|i_s\rangle$ before the readout. This metric, however, does not adequately account for the possibility of leakage. Assume for example, that the excited transmon state $|1\rangle$ can leak to a non-computational state $|j\rangle$ with a large probability. Assume also that the state $|j\rangle$ always mistakenly yields the readout outcome 1_m . In this case, the readout fidelity, defined by Eq. (S27) will not reflect the presence of a leakage error; the fidelity can be close to unity even when the probability of leakage is large. This situation was in fact observed in our recent experiment Ref. [17]. Clearly, the QND fidelity defined in Eq. (S23) is more suitable for quantifying the measurement performance in the context of quantum error correction compared to the readout fidelity defined in Eq. (S27).

We note that the QND fidelity can never exceed the readout fidelity, $\mathcal{Q} \leq \mathcal{F}$. This can be seen by noting that

$$P(i_m|i_s) = P(i_s, i_m|i_s) + \sum_{j_s \neq i_s} P(j_s, i_m|i_s) \geq P(i_s, i_m|i_s) \quad (\text{S28})$$

and using the definitions given by Eqs. (S23) and (S27).

To define readout repeatability – which is a conventional measure of the QND character of readout – we consider a sequence of two back-to-back measurements. We then introduce $P(i_{m2}|j_{m1}, k_s)$ as the probability of the second readout yielding outcome i_{m2} given that the outcome of the first readout is j_{m1} and that the system is prepared in state $|k_s\rangle$. The repeatability is then defined as

$$\mathcal{R} = \frac{1}{2} [P(0_{m2}|0_{m1}, 0_s) + P(1_{m2}|1_{m1}, 1_s)]. \quad (\text{S29})$$

Similarly to the readout fidelity, however, this metric might overlook the leakage as leakage states can be mistakenly assigned to 0 or 1. For applications sensitive to leakage errors, repeatability should thus be replaced with the QND fidelity defined in Eq. (S23). Generally, the QND fidelity does not exceed repeatability, $\mathcal{Q} \leq \mathcal{R}$.

Several recent works [18–20] name the repeatability \mathcal{R} , as defined in Eq. (S29), the “QNDness” or “QND fidelity”. We avoid this label for \mathcal{R} and emphasize that it differs from \mathcal{Q} , which we call the QND fidelity. In the absence of leakage, \mathcal{Q} and \mathcal{R} coincide up to corrections quadratic in error probabilities. However, leakage, which is fatal for quantum error correction, might not be detected by \mathcal{R} , while it is adequately captured by \mathcal{Q} . Therefore, we use QND fidelity defined in Eq. (S23) in our work.

V. DETAILS OF QND FIDELITY MEASUREMENT

A. Residual photon number

To verify that our readout pulse empties the resonator after the measurement, we perform a ring-down experiment. In this experiment, we play a single readout pulse and continue to acquire the demodulated signal after the readout pulse is over. Any photons remaining in the resonator at the end of the pulse will leak out on a timescale of $1/\kappa \approx 85\text{ns}$. We can determine the number of photons remaining in the resonator based on the amplitude of the acquired signal after the pulse ends. To do this, we must calibrate the amplitude of the amplified room-temperature signal to the amplitude of the coherent state inside the resonator. To this end, we first play a continuous-wave tone at the cavity frequency and measure the AC Stark shift on the transmon. In conjunction with the known dispersive shift χ , this tells us the amplitude of the cavity field: $|\alpha|^2 = \delta\omega/\chi$. Once the cavity has reached steady-state, we turn off the drive and acquire the resonator ring-down. We can then convert the known $|\alpha|$ to the amplitude of the signal at our room-temperature digitizer.

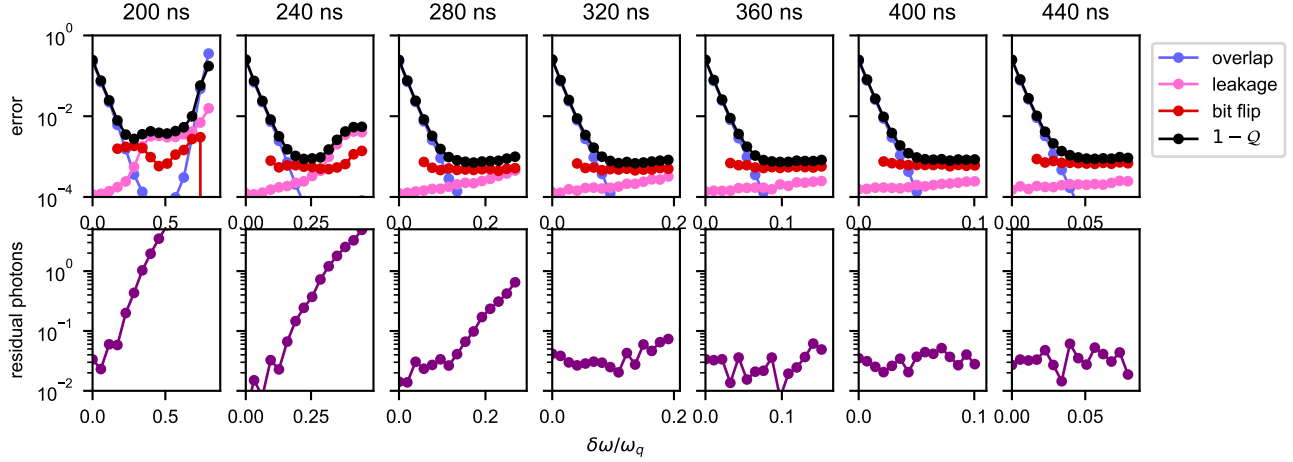


FIG. S6. QND fidelity and residual photon number as a function of readout power and duration.

The performance of our numerically optimized pulses with different durations is demonstrated in Fig. S6. From the figure it is apparent that the pulses are effective at emptying the resonator from photons at the end of the pulse. Only for the shortest pulses with large powers, $\delta\omega/\omega_q \gtrsim 0.2$, does the residual photon number exceed 0.1. This error could be due to our uncertainty on the resonator parameters χ , κ , and nonlinearity K , or it could be due to higher-order nonlinearity.

B. Leakage checks

Here, we discuss the leakage check measurements introduced in the main text. These measurements are intended to detect the escape of qubit state to non-computational states. This detection is achieved by a combination of three strategies. First, we perform the leakage checks in the phase-preserving mode of our quantum limited amplifier. Both quadratures of the signal contain information about leakage. Second, we increase the measurement duration to suppress assignment errors. This allows us to distinguish different non-computational states from each other. Finally, we perform the leakage checks at a lower readout frequency. This improves the contrast between the computational and non-computational states at the cost of sacrificing the contrast between the computational states.

The example histograms of the leakage check measurements are shown in Fig. S7(a,b). It is clear from the figure that the checks distinguish the computational and non-computational states. They moreover distinguish non-computational states $|2\rangle$, $|3\rangle$ and $|4+\rangle$ (where $|4+\rangle$ means $|4\rangle$ or any of the higher states). This resolution allows us to be confident that the leakage transitions that we see in our experiment are unrelated to multi-excitation resonances, which would excite the transmon to states $|4+\rangle$. As demonstrated in Fig. S7(c), the leakage observed in our experiment predominantly leaves the transmon in states $|2\rangle$ and $|3\rangle$.

C. Stability of the QND fidelity with time

Fig. S7(c) also demonstrates that the QND fidelity that we measure is stable for at least 12 hours. This further confirms that our readout is not limited by the multi-excitation resonances. Indeed, we expect the multi-excitation resonances to be strongly sensitive to the offset charge n_g , see Fig. 1(d) of the main text and Fig. S9(b). The offset charge was previously observed to fluctuate on the scale of minutes [21]. We would thus see significant variation of the QND fidelity in our 12-hour sweep if multi-excitation resonances were relevant. In contrast, we see minimal variation with time that can be explained by the drift of the dielectric environment of the qubit.

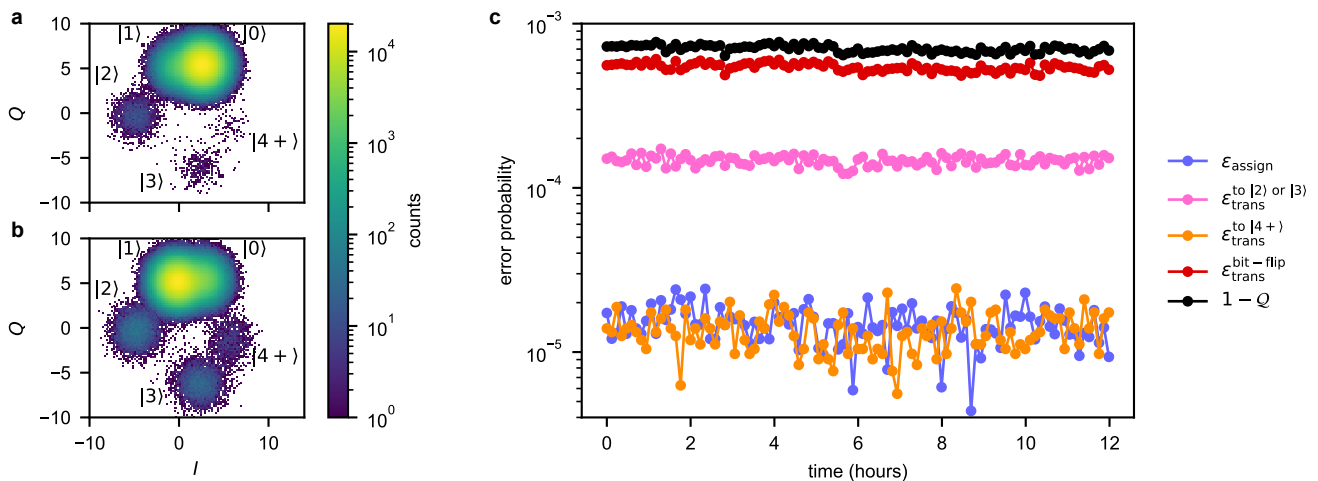


FIG. S7. (a,b) Histogram of leakage check measurement outcomes after the sequence of 18 qubit measurements described in Fig. 4 of the main text. Only shots where qubit began in the computational subspace are shown. In panel (a), the sequences which are not preceded by a π -pulse are shown. In panel (b), sequences which are preceded by a π -pulse are shown. We identify blobs corresponding to transmon states $|0\rangle$ to $|3\rangle$, and a separate blob where states $|4\rangle$ and higher reside. (c) Measurement of QND fidelity over the course of about 12 hours. The measurement is performed using the optimized 320 ns-long pulse discussed in the main text. The QND fidelity remains stable, with most fluctuation arising from changes in the bit-flip rate. This suggests that our leakage errors are not sensitive to offset charge, which typically fluctuates on a timescale of minutes. Most leakage takes the transmon to states $|2\rangle$ and $|3\rangle$. This measurement only places an upper bound on the leakage rate to highly-excited states, since the population in $|4+\rangle$ may be due to a sequence of two excitations over the course of the 18 qubit measurements.

VI. DETAILS OF FLOQUET SIMULATIONS

In this section, we explain the numerical procedure we use to find drive frequencies and powers at which multi-excitation resonances occur. In these simulations, we model the readout signal as a classical monochromatic drive applied to the transmon, following Refs. [22–24]. The resonances can then be identified as regions in the parameter space where the considered computational state appreciably hybridizes with non-computational states due to the presence of the drive. The information about this hybridization is contained in the Floquet modes of the model. To quantify the hybridization, we introduce the quantity

$$\Theta = 1 - |\langle c|\psi\rangle|^2, \quad (\text{S30})$$

where $|c\rangle$ is the Stark-shifted computational state and $|\psi\rangle$ is the Floquet mode which has the highest overlap with $|c\rangle$. Away from multi-excitation resonances $|\psi\rangle \approx |c\rangle$ and Θ is close to zero. In contrast, exactly on resonance, the Floquet mode becomes an equal superposition between the computational state and a non-computational state leading to $\Theta = 1/2$.

Below, we present the full details of our numerical approach. First, we explain how we find the Floquet modes by diagonalizing the propagator over one drive period. Then, to build intuition for this approach, we find the Floquet modes in a simple driven two-level-system model. In this case we can explicitly compute the hybridization Θ . We then detail how our technique applies to the case of a transmon qubit. An additional complication in this case (as compared to the two-level system model) comes from the presence of AC Stark shifts for all transmon levels. We clarify how this effect can be calibrated out. Finally, from numerical simulations, we extract transition amplitudes corresponding to multi-excitation resonances. We show that in our parameter range they can be well captured by a simple analytical expression.

A. Definition of Floquet modes through the propagator

Assume that the system is described by a Hamiltonian $H(t)$ periodic with period T , $H(t+T) = H(t)$. The dynamics of the system can then be decomposed in terms of the Floquet modes, defined as the eigenvectors of the propagator

over one drive period,

$$U(0, T)|\Phi_m\rangle = e^{-i\epsilon_m T/\hbar}|\Phi_m\rangle, \quad U(0, T) = \mathcal{T} \exp\left(-\frac{i}{\hbar} \int_0^T H(t) dt\right). \quad (\text{S31})$$

Here, $|\Phi_m\rangle$ is the Floquet mode indexed by m and ϵ_m is the associated quasienergy. The symbol \mathcal{T} denotes time ordering.

The evolution operator $U(0, T)$ can always be represented in the form $U(0, T) = \exp(-iH_F T/\hbar)$. We call the operator H_F the static effective Hamiltonian. If its explicit form is known, diagonalization of the propagator reduces to that of the static effective Hamiltonian. Otherwise, the Floquet modes can be found by diagonalizing the propagator numerically. For the case of a transmon, we rely on the latter approach.

B. Simple example of identifying resonances via Floquet modes

Here, we present a simple two-level model of a resonance in which the hybridization induced by the drive can be computed analytically. This model demonstrates how the resonances can be identified by finding the Floquet modes and evaluating the hybridization Θ defined in Eq. (S30). The intuition developed here is directly applicable to the case of a driven transmon.

In our two-level model, we take one state to play the role of a computational state $|c\rangle$ and the other that of a non-computational state $|nc\rangle$. The Hamiltonian of the model in the basis $\{|nc\rangle, |c\rangle\}$ is given by

$$\frac{H}{\hbar} = \frac{\omega}{2}(1 + \sigma_z) + \frac{A}{2}(\sigma_+ e^{-i\omega_d t} + \sigma_- e^{i\omega_d t}), \quad (\text{S32})$$

where the σ_- , σ_+ , σ_z are the standard Pauli operators. Within this model, static effective Hamiltonian H_F can be found explicitly by going to the rotating frame,

$$H_F = \frac{\Delta}{2}(\sigma_z + 1) + \frac{A}{2}\sigma_x, \quad \Delta = \omega - \omega_d. \quad (\text{S33})$$

Here, we omitted an unimportant constant term. Diagonalizing the static effective Hamiltonian, we find the quasienergies; they are given by $\epsilon_{\pm}/\hbar = \pm\Omega/2$ with $\Omega = \sqrt{(A/2)^2 + (\Delta/2)^2}$. The associated Floquet modes are given by

$$\begin{aligned} |\epsilon_+\rangle &= \cos(\theta/2)|nc\rangle + \sin(\theta/2)|c\rangle, \\ |\epsilon_-\rangle &= \sin(\theta/2)|nc\rangle - \cos(\theta/2)|c\rangle, \end{aligned} \quad (\text{S34})$$

where $\theta = \arctan(A/\Delta)$. Given these Floquet modes, we can now proceed to compute the hybridization

$$\Theta = 1 - \max(|\langle c|\epsilon_-\rangle|^2, |\langle c|\epsilon_+\rangle|^2) = \frac{(A/\Delta)^2}{2[1 + (A/\Delta)^2 + \sqrt{1 + (A/\Delta)^2}]}. \quad (\text{S35})$$

This function peaks at $1/2$ for $\Delta = 0$, indicating a resonance, see Fig. S8.

C. Using Floquet modes to identify resonances in a transmon qubit

In this section, we elaborate on the numerical procedure for finding resonances in the spectrum of a driven transmon. As explained above, we determine the resonant conditions by computing Floquet modes and using them to compute the hybridization Θ between the computational and non-computational states.

The Hamiltonian of a driven transmon is given by

$$H = 4E_C(N - n_g)^2 - E_J \cos \varphi + \hbar\zeta N \cos(\omega t), \quad (\text{S36})$$

where ω is the readout resonator frequency and ζ is the amplitude of the drive acting on the transmon. The drive amplitude can be related to the induced AC-stark shift $\delta\omega$ by

$$\frac{\delta\omega}{\omega_q} = \frac{1}{8} \frac{\zeta^2 \omega^2}{(\omega^2 - \omega_q^2)^2}, \quad (\text{S37})$$

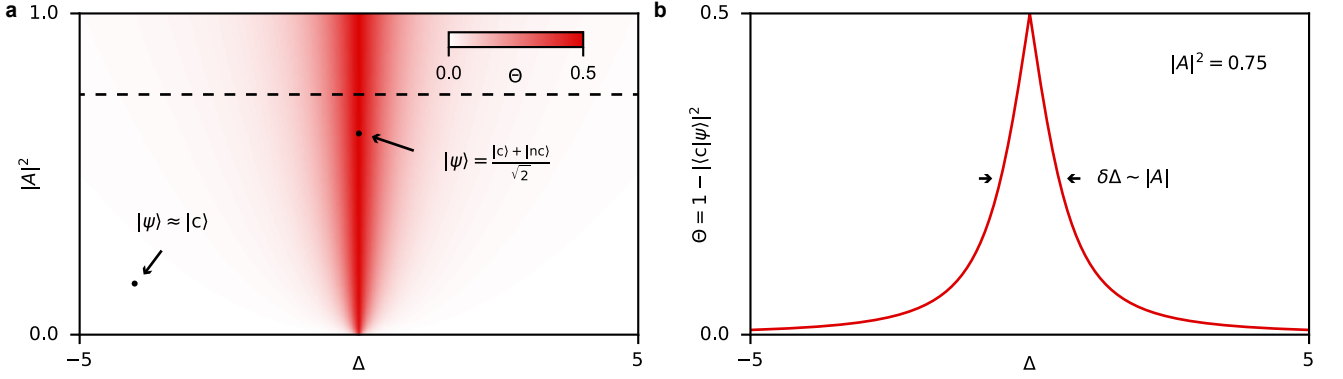


FIG. S8. A drive can induce hybridization between one of the computational states, $|c\rangle$, and a non-computational state $|nc\rangle$. We quantify the degree of hybridization Θ via by computing the squared overlap between the Floquet mode $|\psi\rangle$ closest to $|c\rangle$ and the non-computational state $|nc\rangle$. (a) Hybridization Θ as a function of drive power $|A|^2$ and detuning of the drive Δ from the transition between $|c\rangle$ and $|nc\rangle$ computed within a two-level toy model, see Eq. (S32). Away from resonance, we have $|\Delta| \gg |A|$, thus the Floquet mode is close to $|c\rangle$ resulting in $\Theta \ll 1$. Close to resonance, $|\Delta| \ll |A|$, the Floquet mode is an equal superposition of $|c\rangle$ and $|nc\rangle$ resulting in $\Theta = 1/2$. (b) A cut of panel (a) at $|A|^2 = 0.75$. The width of the resonant feature in $\Theta(\Delta)$ is determined by the drive matrix element $|A|$.

where we assumed $E_J/E_C \gg 1$ and $|\omega - \omega_q| \gg E_C/\hbar$. To pinpoint the combinations of ω and $\delta\omega$ that activate the resonances, we compute the Floquet modes $|\Phi_m\rangle$ associated with Eq. (S36). This can no longer be done analytically: unlike Section VI B, there is no rotating frame eliminating all time dependence in Eq. (S36). For this reason, we resort to computing the Floquet modes numerically using the open-source package QuTiP [25, 26]. This is achieved by diagonalizing the propagator (S31) with $H(t)$ given in Eq. (S36).

There is, however, an important complication not captured by the simple model considered in Section VI B. Namely, under the applied drive, the Floquet modes are AC Stark shifted from the “bare” undriven states. This effect results from the combination of the transmon nonlinearity and the drive; it is present even away from any spurious resonances. In fact, when $\delta\omega \gtrsim E_C/2\hbar$, the Stark-shifted Floquet modes can differ substantially from their undriven counterparts. When computing the hybridization Θ , we should specifically consider the Stark-shifted computational and non-computational states.

To determine the structure of the Stark-shifted states, following Ref. [23], we first identify for each (ζ, ω) the Floquet mode $|\ell(\zeta, \omega)\rangle$ with maximum overlap with the bare undriven transmon state $|\ell\rangle$. We then decompose this Floquet mode in the undriven basis. The decomposition coefficients can be expressed as a power series of ζ and ω :

$$\langle k|\ell(\zeta, \omega)\rangle = \sum_{ij} C_{ijkl} \zeta^i \omega^j. \quad (\text{S38})$$

The decomposition coefficients are determined by fitting the numerically extracted coefficients to a polynomial truncated to $i, j \leq 4$. Importantly, we exclude from this fit any points (ζ, ω) where the overlap between the Floquet mode and any bare “undriven” state is below a threshold (typically taken to be 0.8). This is needed to avoid fitting any spurious resonances.

Because the overlap with the bare state eventually drops below the threshold for a sufficiently strong drive, we perform the above procedure iteratively [23]. We split the drive amplitudes under consideration into multiple windows. In the first window (smallest drive amplitudes), we proceed as above. In the next window, we take as the “bare state” the fitted state from the previous window, and so on. Once all Floquet modes have been extracted and labeled in this way, we perform a final fit over the whole range of drive frequencies and amplitudes to yield a result free from numerical artifacts at the window boundaries.

Having now obtained both the Floquet modes as well as the numerically-fit AC-Stark-shifted computational states, we are now in a position to calculate the hybridization Θ . In this way we obtain Figure 3 of the main text of the manuscript. The code utilized to perform these numerical simulations is available as an open-source Python package `floquet` [27].

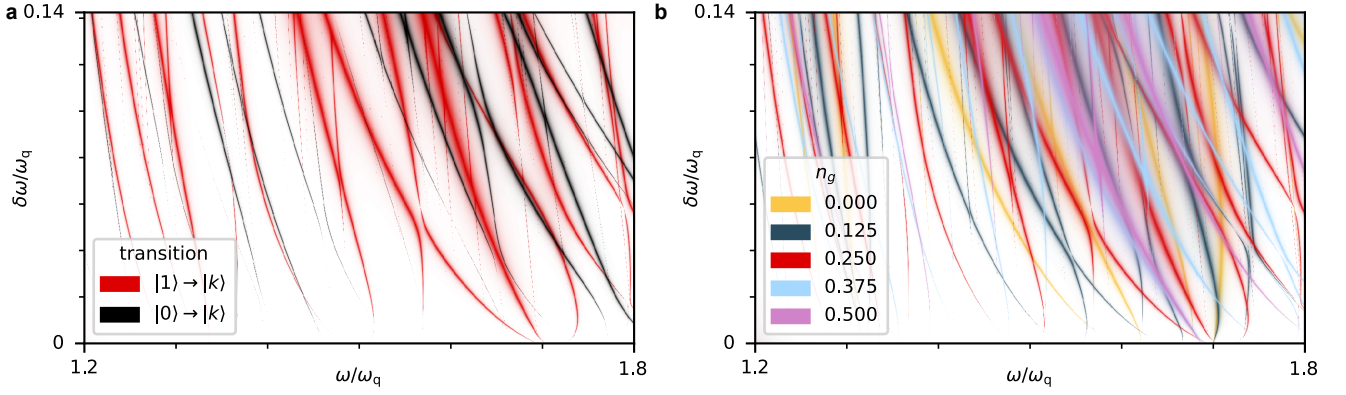


FIG. S9. Multi-excitation resonances for $E_J/E_C = 60$ as a function of drive frequency and power. (a) Multi-excitation resonances for transmon initialized in the ground state (black) and the first excited state (red). Offset charge is set to $n_g = 0.25$. (b) Spectrum of multi-excitation resonances for transmon prepared in the state $|1\rangle$ as a function of the offset charge n_g . The spectrum is highly n_g -dependent.

D. Additional Floquet simulations

Judging from Figure 3 of the main text it may seem that undesired resonances can be avoided in the standard readout regime $\omega_r \sim \omega_q$ by correctly choosing the readout frequency. This strategy is invalidated, however, by two facts. First, the landscape of resonances is different for transmon state $|1\rangle$ – shown in Figure 2 – and for state $|0\rangle$. The landscape of undesired resonances is much more dense if both states are considered simultaneously, see Figure S9(a). Second, the resonances have a pronounced dependence on the offset charge n_g , even when $E_J/E_C = 60$, see Figure S9(b). This is because the majority of resonances hybridize computational states to charge-sensitive states near the top or outside of the Josephson well. Random drifts of n_g with time [21, 28] make it hard to avoid the resonances without a dedicated offset-charge control.

E. Comparison of transition amplitudes between simulation and simple analytical theory

In our regime, the strongest undesired resonances employ one drive photon and excite the qubit to a non-computational state. This happens when the drive frequency ω satisfies $\hbar\omega = E_j - E_i$, where ω is the drive frequency, E_i is the energy of the initial computational transmon state, and E_j is the energy of the final non-computational state. For ω close to the resonance, the hybridization between the computational state and the non-computational state can be described by a 2×2 static effective Hamiltonian

$$H_F = \begin{pmatrix} E_i & \hbar\Omega_{i \rightarrow j} \\ \hbar\Omega_{i \rightarrow j}^* & E_j - \hbar\omega \end{pmatrix}. \quad (\text{S39})$$

Transition amplitude $\Omega_{i \rightarrow j}$ depends on ζ . At small drive powers this dependence is given by

$$\hbar\Omega_{i \rightarrow j}^{\text{low-power}} = \frac{1}{2}\zeta \langle j|N|i \rangle, \quad (\text{S40})$$

At higher powers, $\Omega_{i \rightarrow j}$ deviates from the low-power expression (S40) due to the possibility of reaching the final state through a sequence of intermediate virtual states [29]. To evaluate the importance of these corrections, we extract the transition amplitude $\Omega_{i \rightarrow j}$ from our Floquet numerical simulation. This can equivalently be done either by evaluating the anti-crossing of quasienergies of the Floquet modes corresponding to the considered states or by fitting the hybridization Θ to Eq. (S35). Notably, to numerically find the transition amplitude, it is important to account for the AC Stark shift of energies E_i and E_j .

The result of this procedure is shown in Figure S10. As is apparent from the figure, the corrections to the low-power expression (S40) are small at powers used in our experiment. This justifies the use of Eq. (S40) in the main text when estimating the transition amplitudes. We note that the transitions relevant for our experiment are $|0\rangle \rightarrow |14\rangle$ and $|1\rangle \rightarrow |15\rangle$.

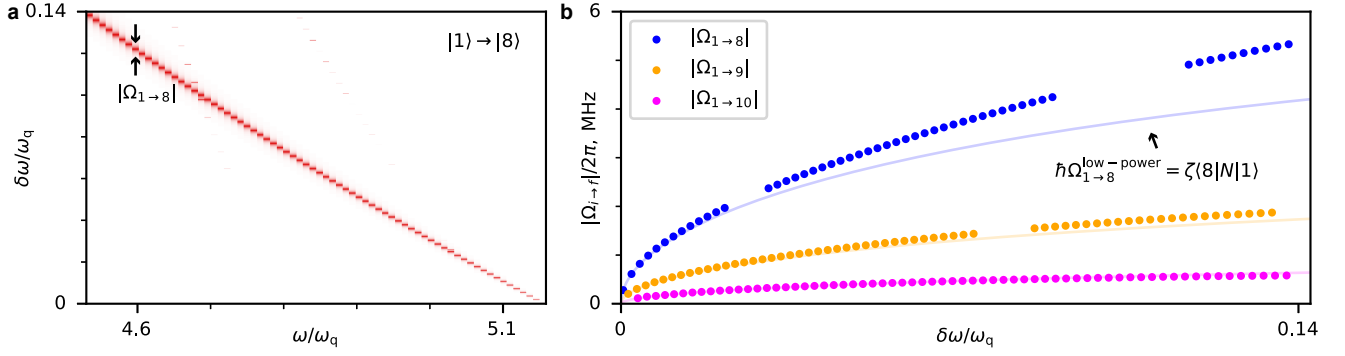


FIG. S10. Transition amplitudes corresponding to the multi-excitation resonances. Parameters used for the plot are same as in Figure 2 of the main text. (a) Hybridization between the computational state $|i\rangle = |1\rangle$ and a non-computational state $|j\rangle = |8\rangle$ as a function of drive power and frequency. The resonant feature occurs when $\hbar\omega = E_8 - E_1$; the width of this feature is determined by the transition amplitude $\Omega_{1\rightarrow 8}$. This allows us to numerically find $\Omega_{1\rightarrow 8}$ as a function of power. (b) Comparison between the low-power expression (S40) for the transition amplitude (solid lines) and the numerically extracted transition amplitudes (dots). Gaps in the numerical data occur where several resonances cross; there Eq. (S39) does not correctly describe the behavior of the system and $\Omega_{i\rightarrow j}$ is ill-defined.

-
- [1] A. P. M. Place, L. V. H. Rodgers, P. Mundada, B. M. Smitham, M. Fitzpatrick, Z. Leng, A. Premkumar, J. Bryon, A. Vrajitoarea, S. Sussman, G. Cheng, T. Madhavan, H. K. Babla, X. H. Le, Y. Gang, B. Jäck, A. Gyenis, N. Yao, R. J. Cava, N. P. de Leon, and A. A. Houck, New material platform for superconducting transmon qubits with coherence times exceeding 0.3 milliseconds, *Nature Communications* **12**, 1779 (2021).
 - [2] S. Ganjam, Y. Wang, Y. Lu, A. Banerjee, C. U. Lei, L. Krayzman, K. Kisslinger, C. Zhou, R. Li, Y. Jia, M. Liu, L. Frunzio, and R. J. Schoelkopf, Surpassing millisecond coherence in on chip superconducting quantum memories by optimizing materials and circuit design, *Nature Communications* **15**, 3687 (2024).
 - [3] K. Serniak, S. Diamond, M. Hays, V. Fatemi, S. Shankar, L. Frunzio, R. Schoelkopf, and M. Devoret, Direct dispersive monitoring of charge parity in offset-charge-sensitive transmons, *Physical Review Applied* **12**, 014052 (2019).
 - [4] T. Connolly, P. D. Kurilovich, S. Diamond, H. Nho, C. G. Böttcher, L. I. Glazman, V. Fatemi, and M. H. Devoret, Coexistence of Nonequilibrium Density and Equilibrium Energy Distribution of Quasiparticles in a Superconducting Qubit, *Physical Review Letters* **132**, 217001 (2024).
 - [5] R. Rehammar and S. Gasparinetti, Low-Pass Filter With Ultrawide Stopband for Quantum Computing Applications, *IEEE Transactions on Microwave Theory and Techniques* **71**, 3075 (2023).
 - [6] E. M. Purcell, H. C. Torrey, and R. V. Pound, Resonance Absorption by Nuclear Magnetic Moments in a Solid, *Physical Review* **69**, 37 (1946).
 - [7] D. Kleppner, Inhibited Spontaneous Emission, *Physical Review Letters* **47**, 233 (1981).
 - [8] P. Goy, J. M. Raimond, M. Gross, and S. Haroche, Observation of Cavity-Enhanced Single-Atom Spontaneous Emission, *Physical Review Letters* **50**, 1903 (1983).
 - [9] A. Blais, R.-S. Huang, A. Wallraff, S. M. Girvin, and R. J. Schoelkopf, Cavity quantum electrodynamics for superconducting electrical circuits: An architecture for quantum computation, *Physical Review A* **69**, 062320 (2004).
 - [10] A. A. Houck, J. A. Schreier, B. R. Johnson, J. M. Chow, J. Koch, J. M. Gambetta, D. I. Schuster, L. Frunzio, M. H. Devoret, S. M. Girvin, and R. J. Schoelkopf, Controlling the Spontaneous Emission of a Superconducting Transmon Qubit, *Physical Review Letters* **101**, 080502 (2008).
 - [11] A. Yen, Y. Ye, K. Peng, J. Wang, G. Cunningham, M. Gingras, B. M. Niedzielski, H. Stickler, K. Serniak, M. E. Schwartz, and K. P. O'Brien, Interferometric Purcell suppression of spontaneous emission in a superconducting qubit (2024), arXiv:2405.10107.
 - [12] J. Koch, T. M. Yu, J. Gambetta, A. A. Houck, D. I. Schuster, J. Majer, A. Blais, M. H. Devoret, S. M. Girvin, and R. J. Schoelkopf, Charge-insensitive qubit design derived from the Cooper pair box, *Physical Review A* **76**, 042319 (2007).
 - [13] V. E. Manucharyan, Ph.D. Thesis, Yale University (2012).
 - [14] G. Zhu, D. G. Ferguson, V. E. Manucharyan, and J. Koch, Circuit QED with fluxonium qubits: Theory of the dispersive regime, *Physical Review B* **87**, 024510 (2013).
 - [15] R. Ruskov and C. Tahan, Longitudinal (curvature) couplings of an N-level qudit to a superconducting resonator at the adiabatic limit and beyond, *Physical Review B* **109**, 245303 (2024).
 - [16] M. F. Gely, G. A. Steele, and D. Bothner, Nature of the Lamb shift in weakly anharmonic atoms: From normal-mode splitting to quantum fluctuations, *Physical Review A* **98**, 053808 (2018).
 - [17] S. Hazra, W. Dai, T. Connolly, P. D. Kurilovich, Z. Wang, L. Frunzio, and M. H. Devoret, Benchmarking the readout of

- a superconducting qubit for repeated measurements (2024), arXiv:2407.10934.
- [18] S. Touzard, A. Kou, N. Frattini, V. Sivak, S. Puri, A. Grimm, L. Frunzio, S. Shankar, and M. Devoret, Gated Conditional Displacement Readout of Superconducting Qubits, *Physical Review Letters* **122**, 080502 (2019).
 - [19] Y. Sunada, S. Kono, J. Ilves, S. Tamate, T. Sugiyama, Y. Tabuchi, and Y. Nakamura, Fast Readout and Reset of a Superconducting Qubit Coupled to a Resonator with an Intrinsic Purcell Filter, *Physical Review Applied* **17**, 044016 (2022).
 - [20] P. A. Spring, L. Milanovic, Y. Sunada, S. Wang, A. F. van Loo, S. Tamate, and Y. Nakamura, Fast multiplexed superconducting qubit readout with intrinsic Purcell filtering (2024), arXiv:2409.04967 [quant-ph].
 - [21] K. Serniak, M. Hays, G. de Lange, S. Diamond, S. Shankar, L. Burkhardt, L. Frunzio, M. Houzet, and M. Devoret, Hot nonequilibrium quasiparticles in transmon qubits, *Physical Review Letters* **121**, 157701 (2018).
 - [22] R. Shillito, A. Petrescu, J. Cohen, J. Beall, M. Hauru, M. Ganahl, A. G. Lewis, G. Vidal, and A. Blais, Dynamics of Transmon Ionization, *Physical Review Applied* **18**, 034031 (2022).
 - [23] X. Xiao, J. Venkatraman, R. G. Cortiñas, S. Chowdhury, and M. H. Devoret, A diagrammatic method to compute the effective Hamiltonian of driven nonlinear oscillators (2023), arXiv:2304.13656.
 - [24] M. F. Dumas, B. Groleau-Paré, A. McDonald, M. H. Muñoz-Arias, C. Lledó, B. D’Anjou, and A. Blais, Measurement-Induced Transmon Ionization, *Physical Review X* **14**, 041023 (2024).
 - [25] J. R. Johansson, P. D. Nation, and F. Nori, QuTiP: An open-source Python framework for the dynamics of open quantum systems, *Computer Physics Communications* **183**, 1760 (2012).
 - [26] J. R. Johansson, P. D. Nation, and F. Nori, QuTiP 2: A Python framework for the dynamics of open quantum systems, *Computer Physics Communications* **184**, 1234 (2013).
 - [27] D. K. Weiss, *floquet*.
 - [28] D. Ristè, C. C. Bultink, M. J. Tiggelman, R. N. Schouten, K. W. Lehnert, and L. DiCarlo, Millisecond charge-parity fluctuations and induced decoherence in a superconducting transmon qubit, *Nature Communications* **4**, 1913 (2013).
 - [29] D. Sank, Z. Chen, and M. Khezri et al., Measurement-Induced State Transitions in a Superconducting Qubit: Beyond the Rotating Wave Approximation, *Physical Review Letters* **117**, 190503 (2016).